Available online at www.sciencedirect.com

ScienceDirect

Advances in Space Research 77 (2026) 4121–4151

ADVANCES IN SPACE RESEARCH (a COSPAR publication)

www.elsevier.com/locate/asr

A path towards effective exploitation of quantum sensors in future satellite gravity missions

João Encarnação [a,*], Christian Siemes [a], Ilias Daras [b], Olivier Carraz [b], Aaron Strangfeld [b], Philipp Zingerle [c], Roland Pail [c]

[a] Delft University of Technology, Kluyverweg 1, 2629 HS Delft, the Netherlands
[b] European Space Research and Technology Centre, Keplerlaan 1, 2200 AG Noordwijk, the Netherlands
[c] Technical University of Munich, Arcisstraße 21, D-80333 Munich, Germany

Received 5 August 2025; received in revised form 16 November 2025; accepted 14 December 2025
Available online 17 December 2025

Abstract

Mapping the Earth's gravity field from space provides valuable insights into climate change, the evolution of the hydro- and biosphere, and seismic activity. Current satellite gravimetry missions have demonstrated the utility of gravity data in understanding global mass transport phenomena, climate dynamics, and geological processes. However, state-of-the-art measurement techniques face limitations due to noise and long-term drift, which propagate into the recovery of Earth's time-varying gravity field. Quantum sensors, particularly Cold Atom Interferometry (CAI), offer promise for improving the accuracy and stability of space-based gravity measurements. Therefore, CAI has emerged as a promising measurement technique for future gravimetric satellite missions due to its potential for measuring gravitational forces and gradients with high precision and accuracy, particularly at low frequencies (sub-mHz). This study examines the sensitivity of CAI accelerometers and gradiometers to errors in measuring the satellite's attitude and compares it to that of state-of-the-art traditional electrostatic accelerometers. We explore the low-low satellite-to-satellite and gravity gradiometry concepts and build the respective analytical models of measurements and associated errors. We selected an ambitious scenario for CAI parameters that illustrates a potential path for increasing the accuracy of this type of instrument and its related capabilities for space gravimetry. Two operational modes, concurrent (where a new cloud is generated while another is moved to the interferometric chamber) and sequential (where cloud generation and interferometry happen in the same place), are compared to mitigate the effects of inaccurately known attitude rates on Coriolis accelerations. The sequential mode shows potential to reduce these effects, as the atom cloud initially has zero velocity. Otherwise, the Coriolis effects are dominant in the concurrent operational mode. We additionally consider the impact on attitude uncertainty in the context of errors related to the reference frame rotation from the body to the Earth's co-rotating frames. In addition to the accuracy of attitude measurement, this aspect also highlights the need for drag-free compensation due to the interplay between imperfect frame rotations and the amplitude of the non-gravitational signal. The CAI configuration considered in this study enables the observation of the time-variable gravity signal in the case of low-low Satellite-to-Satellite Tracking missions. Still, it is insufficient for gravity gradient missions because of the reduced signal amplitude. We find it essential to understand and navigate the inherent technical challenges associated with quantum sensors in order to secure an efficient path towards exploiting this technology to monitor changes in the gravity field.

Keywords: Temporal Gravity Field; Cold Atom Interferometry; Gradiometry; low-low Satellite-to-Satellite Tracking; Accelerometer

* Corresponding author.
E-mail addresses: J.G.deTeixeiradaEncarnacao@tudelft.nl (J. Encarnação), C.Siemes@tudelft.nl (C. Siemes), Ilias.Daras@esa.int (I. Daras), olivier.carraz@esa.int (O. Carraz), Aaron.Strangfeld@esa.int (A. Strangfeld), zingerle@tum.de (P. Zingerle), roland.pail@tum.de (R. Pail).

https://doi.org/10.1016/j.asr.2025.12.053
0273-1177/

Abbreviations and Acronyms

AOHIS Atmosphere, Ocean, Hydrology, Ice and Solid-Earth
ASD Amplitude Spectral Density
BEC Bose-Einstein Condensate
CAI Cold Atom Interferometer/interferometry
CARIOQA Cold Atom Rubidium Interferometer in Orbit for Quantum Accelerometry
CoM Centre of Mass
DKC Delta Kick-Collimation
DFC Drag-Free Control
DLR German Aerospace Center
DWS Differential wavefront sensor
ECEF Earth-centred, Earth-fixed (reference frame)
ECI Earth-centred, inertial (reference frame)
ESA European Space Agency
GG Gravity Gradiometry/gradiometer
GFZ GeoForschungsZentrum
GNSS Global Navigation Satellite System
GOCE Gravity field and steady-state Ocean Circulation Explorer
GRACE Gravity Recovery and Climate Experiment
GRACE-C GRACE-Continuity
GRACE-FO GRACE Follow-On
IMU Inertial Measurement Unit
ISR Inter-satellite range/ranging
KBR K-Band Ranging
LEO Low-Earth Orbit
LHRF Local Horizontal Reference Frame
LISA Laser Interferometer Space Antenna
LOS Line-Of-Sight
LRI Laser Ranging Interferometer
LTI Laser Tracking Instrument
ll-SST low-low Satellite-to-Satellite Tracking
NASA National Aeronautics and Space Administration
μASC Micro Advanced Stellar Compass
MOT Magneto-Optical Trap
NGGM Next Generation Gravity Mission
QSG Quantum Space Gravimetry
QSG4EMT QSG for monitoring Earth Mass Transport processes
PSD Power Spectral Density
RMS Root Mean Square
SH Spherical Harmonic
STD Standard Deviation
SRF Satellite Reference Frame
SWAP Size, Weight, and Power
TMA Triple Mirror Assembly
USO Ultra-Stable Oscillator

1. Introduction

Recent advancements in quantum technology (Belenchia et al., 2022; Benyoucef, 2025) have spurred interest in developing highly sensitive instruments for gravitational measurements from space. Among these instruments, Cold Atom Interferometry (CAI) accelerometers and gradiometers are promising due to their potential for observing gravitational forces and gradients with high precision and accuracy. The microgravity environment in space allows for substantially longer interrogation time than on the ground, which is currently a limitation in developing these instruments.

The European Commission, backed by several European countries, has recently announced substantial investments in quantum technology to tackle contemporary digital challenges, including secure communication and computing power. Europe has been at the forefront of spaceborne quantum sensor development since the early 2000s, with initiatives such as the *Interférométrie atomique à sources Cohérentes pour l'Espace* and *Matter-Wave Interferometry in Weightlessness* (Becker et al., 2018) advancing the field. The development of quantum sensors requires close collaboration between academia, industry, and space agencies to overcome technological challenges and prepare for future space missions (Kaltenbaek et al., 2021). Furthermore, integrating quantum sensors into space missions may enhance Earth observation and facilitate the exploration of celestial bodies, such as the Moon and Mars, ushering in a new era of space science and technology (Abend et al., 2023).

Mapping the Earth's gravity field from space offers unique insights into climate change, the evolution of the hydro- and cryosphere (Groh et al., 2019; Jiang et al., 2014), seismic activity monitoring and modeling (Han, 2006), among other applications. Past satellite gravimetry missions, such as NASA and DLR's Gravity Recovery and Climate Experiment (GRACE), NASA and GFZ Helmholtz Centre for Geosciences' GRACE Follow-On (GRACE-FO) and ESA's Gravity Field and Steady-State Ocean Circulation Explorer (GOCE), have demonstrated the importance and relevance of gravity data in understanding global mass transport phenomena, climate dynamics, and geological processes. However, classical measurement techniques face limitations regarding noise and drift, which hinder the recovery of Earth's time-varying gravity field. ESA's Next Generation Gravity Mission (NGGM) and NASA and DLR's GRACE-Continuity (GRACE-C) mission are poised to leverage classical sensors to enhance Earth observation capabilities (Massotti

et al., 2021; Cesare et al., 2022; Heller-Kaikov et al., 2023). The advent of quantum sensors, particularly CAI technology, holds promise for improving the accuracy and stability of space-based gravity measurements. Unlike some studies of spaceborne CAI (e.g., Zhu et al., 2022), we focus on the requirements for resolving the Atmosphere, Ocean, Hydrology, Ice and Solid-Earth (AOHIS) components of the time-variable gravity field model (Dobslaw et al., 2016).

While we are not proposing any specific mission configuration, we consider two measurement concepts: changes in the range between two satellites orbiting in formation, a technique called low-low Satellite-to-Satellite (ll-SST), and in situ gravity gradients collected by a gradiometer onboard a single satellite, called Gravity Gradiometry (GG). In the case of ll-SST, the changes in the inter-satellite range (ISR), which is the *main observable*, are caused by gravity and non-gravitational accelerations affecting the motion of the satellites. This measurement concept requires accelerometers to be placed at the centre of mass (CoM) of the satellite, thereby making them sensitive to non-gravitational accelerations and allowing gravitational accelerations to be isolated during data processing on the ground. In the case of GG, the gradiometer comprises one or more pairs of accelerometers, and their differential acceleration measurements, which are the *main observable here*, are related to the gravity gradient at the satellite's location. We only consider these measurement concepts because we assume they could be realised within the next two decades. It is in this period that CAI technology will most likely mature into a primary sensor for collecting non-gravitational or gravity gradient observations. In this context, making an informed decision about which measurement concept is best suited to CAI technology, given the current and foreseeable technological limitations of all relevant on-board sensors, is an important aspect to clarify.

We designate the accelerometers onboard current and past gravimetric missions by electrostatic instruments, cf. Section 2.3.1 and quantum instruments are further discussed in Section 2.3.2. We evaluate the ll-SST and GG with both electrostatic and quantum instruments to quantify the added value of the latter in contrast to the state-of-the-art of the former. It is essential to determine how far the current level of CAI technology is from becoming the optimal choice for future gravimetric missions.

Associated with the measured physical quantities of these measurement concepts are their respective *product noise*, whose quantification in the spectral domain is the focus of this study. It is a prediction of the accuracy of the actual gravimetric observation that is exploited to produce a gravity field solution, but excluding the errors in models of 1) well-known gravity signals such as tidal accelerations and 2) high-frequency signals that cannot be measured, such as non-tidal atmospheric and ocean gravity variations, also known as temporal aliasing. We do not consider any model errors in this study, as they have the same magnitude regardless of the gravimetric sensor accuracy. The product noise differs from the aforementioned main observables, i.e., ISR for ll-SST and differential accelerations for GG. The main observables must be processed to isolate the gravity signal, to which other instruments are critical, notably the attitude and position relative to Earth. Therefore, the accuracy of the product noise is a function of the sensitivity of all relevant sensors and auxiliary instruments, not only of the instrument collecting the main observable.

To maintain a clear focus on the instrument design and limit the scope, we perform no further analyses of the impact of the developed instrument noise models on concrete satellite gravity missions. For that, we refer to Zingerle et al. (2024), who present the propagation of the predicted noise spectra to the gravity field coefficients. That study puts the sensor errors in context with other sources of errors that we are unable to consider, notably model errors. It presents a broad collection of possible future satellite gravity constellation scenarios. Both studies are part of the same ESA Quantum Space Gravimetry for monitoring Earth Mass Transport processes (QSG4EMT) project; see acknowledgments. The results presented in this study are part of the sensitivity analysis of quantum instrument performances, which was fed into the trade space analysis of Quantum Space Gravimetry (QSG) mission architectures in conjunction with a consolidated user requirements database for future QSG missions.

We describe the errors in frequency with the Amplitude Spectral Density (ASD), which is the square root of Power Spectral Density (PSD), denoted by the symbol s in the relevant equations. We start with the listing of instrument noise in Section 2, to collect existing or expected error spectra of all relevant sensors, i.e., attitude (Section 2.1), ISR (Section 2.2), classical and quantum accelerometers (Section 2.3) and discuss the consequences to GG and motivate why we do not consider classical GG (Section 2.4). With a suitable collection of error spectra, we proceed with describing how to quantify the product noise for ll-SST (Section 3) and GG (Section 4). We describe our model for the errors in the quantum accelerometers in Section 3.2.1 as well how the Coriolis accelerations contribute to them, in the context of ll-SST. In Sections 4.2.1 and 4.2.2, we expand this discussion to GG, regarding errors in the CAI gradiometer and rotational effects, respectively. We describe the impact of imperfect attitude reconstruction in the product noise of ll-SST (Section 3.3) and GG (Section 4.3). The importance of the frame acceleration errors is quantified in Section 5.1. We quantify the full error spectra for classical (Section 5.2.1) and quantum (Section 5.2.2) accelerometers for ll-SST, and quantify the challenges with CAI GG in Section 5.3.

One limitation of previous studies is that they ignore the spectral properties of the errors (e.g., Stray et al., 2025). Although that may be the case for the quantum projection noise, the attitude sensors needed to measure and remove the frame rotation effects do not have white noise. It is of critical importance to include the relevant part of the spec-

trum, ranging from 0.2 mHz, related to orbital frequency, to 20 mHz (preferably higher), related to spherical harmonic (SH) degree 113. Other studies have considered the spectral amplitude of the estimated errors, but these were produced under the assumption of white noise for the angular rotation errors (Romeshkani et al., 2025; HosseiniArani et al., 2025) The topic of CAI satellite gradiometry under numerous relevant scenarios and in great detail has been analyzed by Mu et al. (2024) but without considering the effect of attitude errors on the Coriolis accelerations. Some studies focus on the (closed-loop) error propagation of assumed CAI accelerometers or the hybrid of electrostatic and CAI accelerometers to gravity field parameters, with special emphasis on the critical effect of temporal aliasing, without explicitly including frame effects (e.g., Abrykosov et al., 2019; Luthcke et al., 2021). The impact of frame accelerations on the phase measurements has been analysed in Beaufils et al. (2023), where it was shown not to be significant relative to the quantum projection noise of a CAI instrument similar to that predicted to be in the Cold Atom Rubidium Interferometer in Orbit for Quantum Accelerometry (CARIOQA) Quantum Pathfinder Mission (Lévèque et al., 2023). Unlike that study, we assume: i) that the initial position of the atom cloud is at the CoM, to limit the effects from Gravity Gradients and Euler angular accelerations, ii) the (additional) case where the atom cloud moves through the interferometric chamber to allow for a higher rate of measurements and iii) consider CAI instrument parameters that have the potential for future ll-SST and gravity gradient measurement concepts to be superior to current ones.

This study intends primarily to evaluate the effect of current attitude measurement technology on the gravimetric observations collected with CAI. More specifically, we investigate the impact of an inaccurately known attitude on the Coriolis accelerations and propose mitigation strategies. We also quantify the effect of reference frame transformations of the measurements in the presence of inaccurate attitude information. With this, we intend to lay the groundwork for future developments in quantum gravimetry and, consequently, future satellite missions. We achieve this with an emphasis on the sensitivity of CAI instruments to the satellite's angular velocity and demonstrate how to leverage advancements in laser metrology to optimize the benefits of predicted higher accuracy in quantum accelerometers.

Regarding notations, we use capital bold symbols for matrix quantities, non-capital bold symbols for vector quantities, and non-bold symbols for scalar quantities.

2. Instrument specifications

The errors with which an instrument makes a measurement are intrinsic to its design, measurement principle, and construction. These errors are often predicted as part of the instrument's specifications, but they are generally validated through actual measurements. In the case of instruments that do not yet exist, this error takes the form of a requirement, which reflects both the goal accuracy and the feasibility of achieving it. The measured quantities are usually not very useful by themselves, and additional instruments are needed to measure auxiliary observations, thereby fully exploiting the information content of the main instruments. One example of an auxiliary observation is attitude, which is required to project the accelerometer measurements to the Line-Of-Sight (LOS) direction, where the ISR is implicitly defined, in the case of ll-SST, and to reduce the differential accelerometer measurements from frame accelerations in the case of GG.

We present in this section the noise ASD of all main instruments we consider in this study, including the K-band ranging instrument (KBR), Laser Ranging Interferometer (LRI), electrostatic accelerometers, and predicted CAI instruments, as well as instruments that collected auxiliary observations, such as the star sensors, differential wavefront sensors (DWS), and laser gyroscopes. Without being specific to which ll-SST or GG measurement principle they are relevant to, we group these instruments in attitude, ranging, and electrostatic and quantum accelerometers.

We provide a non-exhaustive list of sensors that represent state-of-the-art technology. In the case of the ll-SST, we also offer the expected performance of the laser ranging instrument in the foreseeable future. We do the same for the classic accelerometer in the form of NGGM's "goal" requirement and the MicroSTAR instrument to fly on NGGM (cf. Section 2.3.1). Naturally, we consider quantum instruments that will provide sufficient improvement over classical instruments. Section 2.3.2 describes our error model, and Section 2.3.3 motivates the choice of the relevant CAI parameters. We do not consider future attitude instruments because we do not find substantial improvements in these instruments in the literature. We mitigate this aspect by quantifying the required accuracy to properly exploit the observations collected by the quantum instruments in Section 0.

Multiple sensors that measure the same quantity may be installed in future gravimetric missions. In that case, we assume that m different instruments with error spectra are combined optimally:

$$s^2(f) = \left(\sum_{m=1}^{M} s_m^{-2}(f) \right)^{-1}. \tag{1}$$

Here, $s_m(f)$ is the noise ASD of sensor m, and $s(f)$ is the noise ASD when all sensors are combined optimally. We use the symbol s to identify frequency-dependent errors, even if we omit the frequency dependency.

Integration or differentiation of the noise ASD of a quantity requires the factor $2\pi f$ or its inverse, respectively. In the general case of the n-th derivative ($n > 0$) or n-th integral ($n < 0$), using Lagrange's notation for differentiation and antidifferentiation:

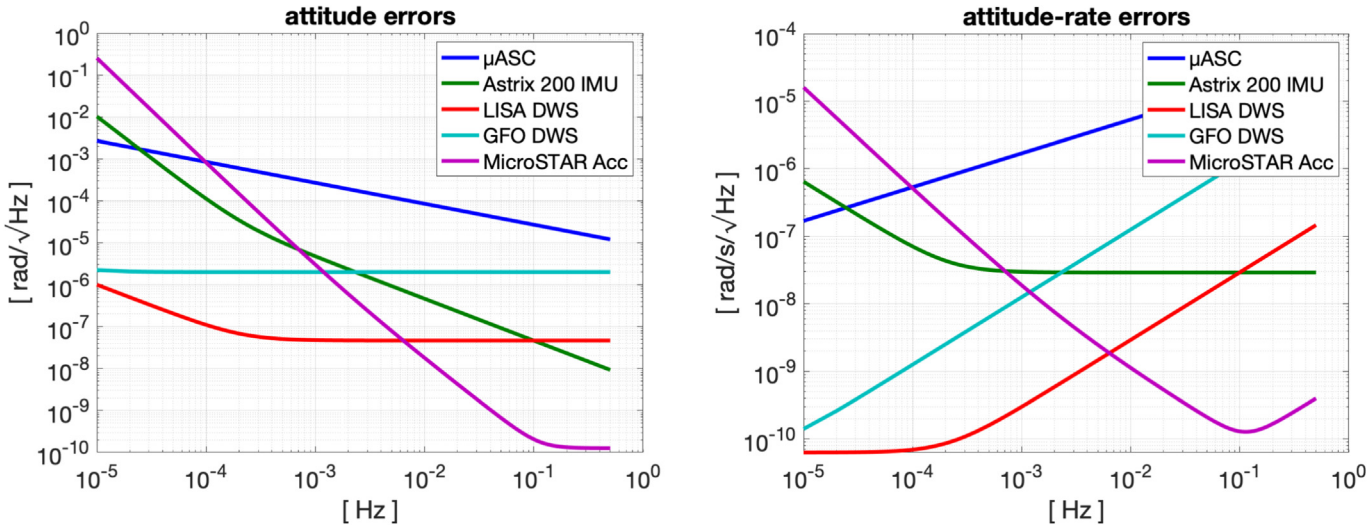

Fig. 1. Overview of attitude errors in terms of attitude (left) and angular rates (right).

$$s\left(f^{(n)}\right) = (2\pi f)^n s(f). \tag{2}$$

2.1. Attitude sensors

This section presents the noise ASD of the attitude instruments considered in the study. We present a wide selection of attitude instruments to assess what is technically feasible in the foreseeable future. Fig. 1 shows an overview of the attitude noise ASDs, where all quantities have been converted to attitude (left) and angular rates (right) for convenience.

To clarify our notation, the symbols s_θ, s_ω and $s_{\dot{\omega}}$ relate to angular error, angular rate error, and angular acceleration error, respectively.

The error spectra we consider are related to the accuracy with which the spacecraft's attitude is known in inertial space. Without going into detail, we assume that the attitude control and any necessary actuators are adequate to maintain the optimal operation of all instruments.

We do not consider quantum attitude sensors, such as those proposed by (Li et al., 2025), because they have a comparatively low resolution (tens of μrad/s), which is higher than that of state-of-the-art commercial inertial measurement units (IMU), which typically have a noise floor at a few tens of nrad/s. Furthermore, the obvious 3D quantum attitude instrument would be very complex, as illustrated in Section 4.2.2.

2.1.1. Star tracker

The star sensor of the Swarm satellites is the Micro Advanced Stellar Compass (μASC) (Herceg et al., 2017). We believe that this instrument is a representative state-of-the-art star sensor. (Goswami et al. 2021) analysed its in-flight accuracy and specified that the noise ASD as

$$s_{\mu\mathrm{ASC},[\mathrm{GRKSLT}]}(f) = 8.5 \times 10^{-6}\sqrt{f^{-1}}\left[\frac{\mathrm{rad}}{\sqrt{\mathrm{Hz}}}\right] \tag{3}$$

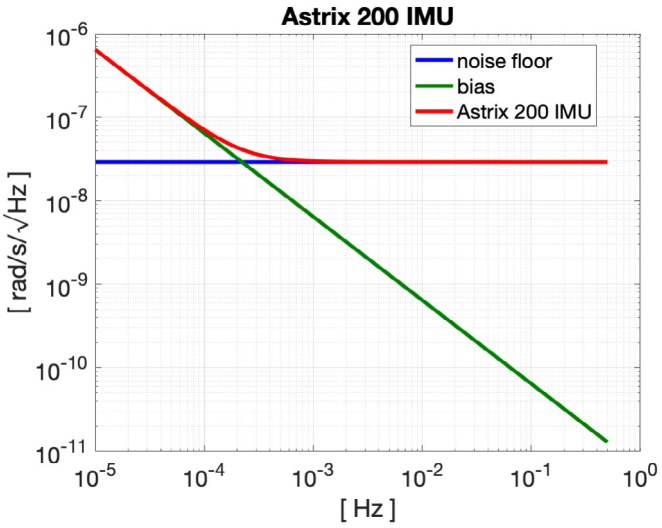

Fig. 2. ASD of the angular velocity noise of the Astrix 200 IMU as inferred from the specification sheet (Airbus, 2022).

2.1.2. Inertial measurement unit

One of the most accurate IMUs is the Astrix 200 laser gyroscope, the accuracy of which is specified in its datasheet (Airbus, 2022). It has a white noise component of 3×10^{-8} rad/s, which is twice as small as what HosseiniArani et al. (2025) considered, and a f^{-1} component associated with bias drift, as shown in Fig. 2. The combined analytical expression is

$$s_{\mathrm{IMU},\omega}(f) = 3 \times 10^{-8}\sqrt{1 + 4.6 \times 10^{-8} f^{-2}}\left[\frac{\mathrm{rad/s}}{\sqrt{\mathrm{Hz}}}\right] \tag{4}$$

Although there are laser gyroscopes with accuracy at 3×10^{-10}rad/s (Stedman et al., 2003), they are not suitable for operation in space.

2.1.3. Differential wavefront sensor

The DWS measures pitch and yaw relative to the LRI. In combination with the Global Navigation Satellite System (GNSS)-derived positions, it is possible to derive the absolute pitch and yaw attitude of the satellite because the GNSS positions provide the absolute attitude of the vector connecting the two satellites. The DWS noise spectra are provided for two cases in the following sections. As for the positioning errors in GNSS s_{GNSS}, they proportionally affect the attitude error in the LOS unit vector $s_{\mathrm{LOS},\theta}$. We assume a white noise with an amplitude of 1 cm/$\sqrt{\mathrm{Hz}}$ as is usually done in preliminary gravimetric studies. Finally, this effect is dampened proportionally to the inter-satellite distance L_{ISR}, assumed to be 200 km:

$$s_{\mathrm{LOS,[GRKSLT]}} = \frac{s_{\mathrm{GNSS}}}{L_{\mathrm{ISR}}} \cong 5 \times 10^{-8} \left[\frac{\mathrm{rad}}{\sqrt{\mathrm{Hz}}}\right]. \tag{5}$$

We consider the DWS from GRACE-FO, Section 2.1.3.2, and from the Laser Interferometer Space Antenna (LISA), Section 2.1.3.2.

2.1.3.1. LISA. As shown in Fig. 3, the noise ASD of the DWS of LISA is composed of the white noise floor (solid blue line) at the level of 10 nrad/$\sqrt{Hz}$ between 1 mHz and 1 Hz and the thermal noise (dotted yellow line) with a spectrum of 1/f below 1 mHz (Schütze et al., 2013).

2.1.3.2. GRACE-FO. Referring to Fig. 3, for GRACE-FO, it is also possible to derive an estimate for the DWS-derived pitch and yaw attitude errors considering the white noise floor (red line), which has an amplitude of 2 µrad/$\sqrt{\mathrm{Hz}}$ (Goswami et al., 2021). The thermal noise floor (dotted yellow line) and the attitude error of the LOS unit vector (dot-dashed purple line) are assumed to be equal to the LISA case in Section 2.1.3.1. The noise floor of the DWS sensor dominates over the GNSS and thermal components, in contrast to the DWS of LISA.

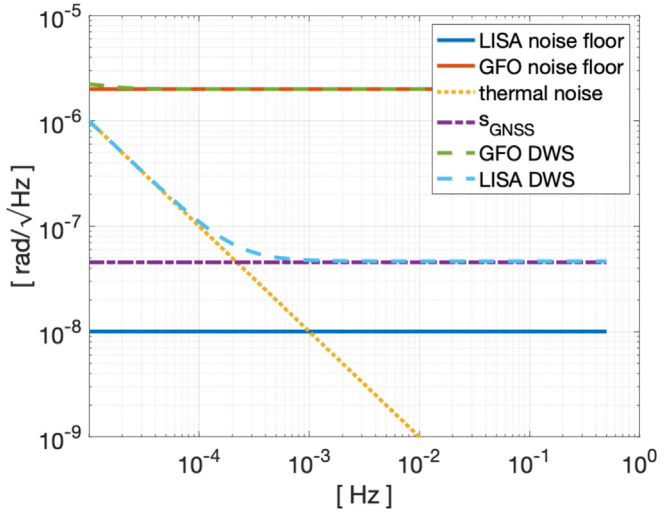

Fig. 3. ASD of the noise floor of the DWS of LISA, solid blue line, (Schütze et al., 2013) and of the DWS of GRACE-FO, solid red line, (Goswami et al., 2021). The dashed green and teal lines represent the ASD of the attitude errors of the DWS of GRACE-FO and LISA, respectively, considering the effects of both GNSS errors, dot-dashed purple line, and thermal noise, dotted yellow line, (Schütze et al., 2013).

2.1.4. Accelerometer-derived attitude

Since each facet of the proof-mass cavity contains multiple electrodes, the MicroSTAR accelerometer can measure angular accelerations. The analytical expression for the error ASD is (Steiger et al., 2014):

$$s_{\mathrm{MicroSTAR},\dot{\omega}}(f) = 1 \times 10^{-10} \times \sqrt{0.4 + 0.001 f^{-1} + 2500 f^{4}} \left[\frac{\mathrm{rad}/s^{2}}{\sqrt{\mathrm{Hz}}}\right]. \tag{6}$$

We assume this noise ASD is the same for all three axes, considering a cubic proof mass, identical gaps between the proof mass and electrodes on all sides, and neglecting the influence of the gold wire connected to the proof mass, which is needed to neutralize the build-up of static charge.

2.2. Inter-satellite ranging

This section presents the noise ASD of the ISR instruments considered in the study. The overview of the noise ASD is shown in Fig. 4.

As we intend to quantify the errors for quantum gravimetric missions, which are currently in the early stages of development, we consider the error spectra associated with the *NGGM 2040* scenario (cf. Section 2.2.4). We report numerous other scenarios for the ranging instrument to contextualise our assumptions with existing instruments and assumptions in the literature.

2.2.1. GRACE-FO KBR

The KBR system is composed of thermal and Ultra-Stable Oscillator (USO)-related components (Sheard et al., 2012), illustrated in Fig. 5 and described by the analytical expression:

$$s_{\mathrm{KBR},\rho} = s_{\mathrm{KBR,thermal}} + s_{\mathrm{KBR,USO}}(f) = 1.4 \times 10^{-6} \left[\frac{m}{\sqrt{Hz}}\right] + 1.8 \times 10^{-8} f^{-\frac{1}{1.6}} \left[\frac{m}{\sqrt{Hz}}\right] \tag{7}$$

2.2.2. GRACE-FO LRI

The noise ASD of the LRI of the GRACE-FO mission is given by the following analytical expression in terms of range noise (Kornfeld et al., 2019), shown as the green line in Fig. 4:

$$s_{\mathrm{LRI},\rho}(f) = 8 \times 10^{-8} \sqrt{1 + (f/0.003)^{-2}} \times \sqrt{1 + (f/0.01)^{-2}} \left[\frac{m}{\sqrt{Hz}}\right]. \tag{8}$$

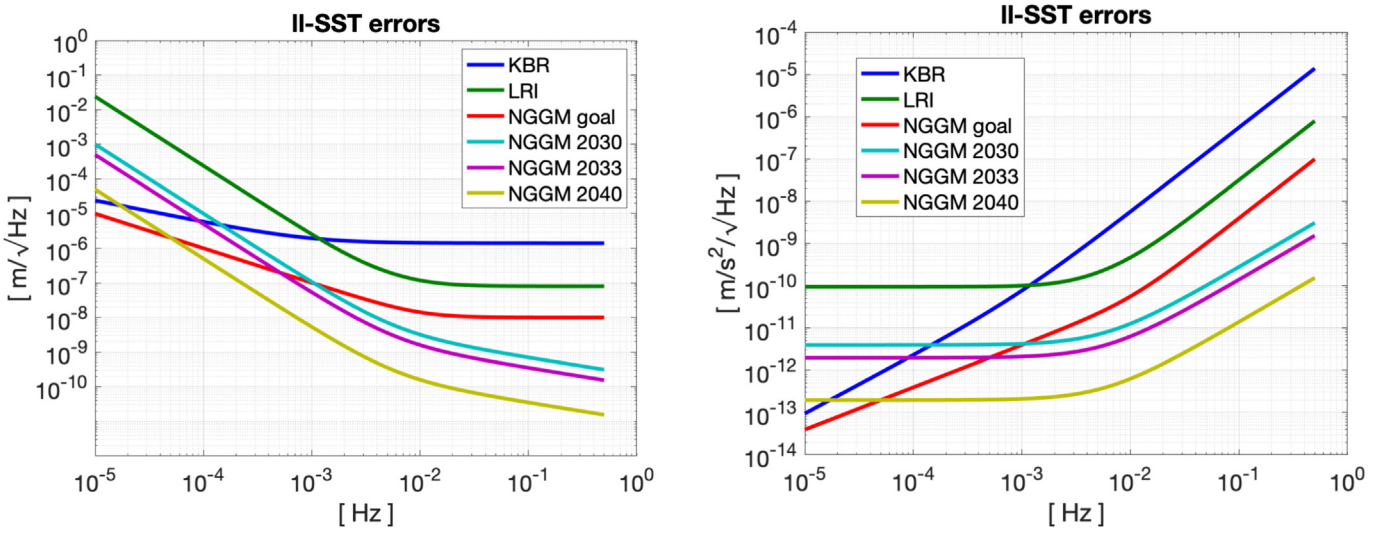

Fig. 4. Overview of ISR noise ASD at the level of distance (left) and acceleration (right).

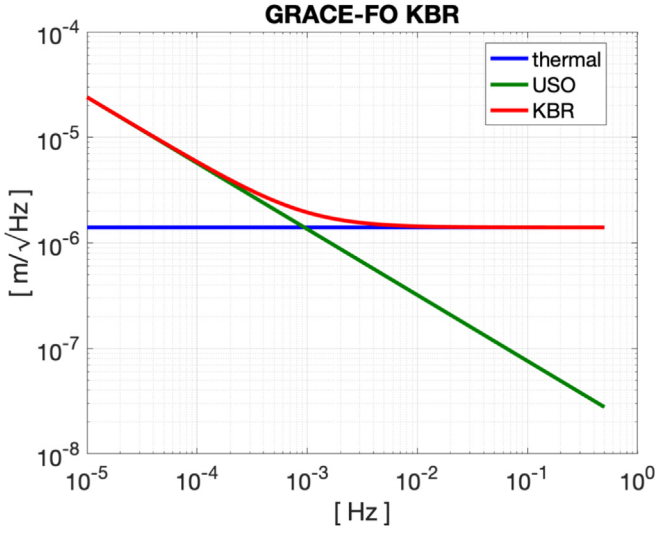

Fig. 5. Noise ASD of the GRACE-FO KBR (Sheard et al., 2012, Fig. 2).

2.2.3. NGGM "goal" laser tracking instrument

The ISR sensors presented so far are indicative of the existing instruments. A comparison between these and future QSG would not correctly represent the capabilities of the former. For that reason, we include in this study the "goal" performance of the Laser Tracking Instrument (LTI) in the NGGM mission concept (Massotti et al., 2021). The associated analytical expression is a function of the inter-satellite distance L_{ISR} (cf. red line in Fig. 4):

$$s_{\mathrm{NGGM},\rho}(f) = L_{\mathrm{ISR}}\, 10^{-13}\sqrt{1+(0.01/f)^2} \times \sqrt{1+(0.001/f)^2}\,\left[\frac{m}{\sqrt{Hz}}\right]. \quad (9)$$

2.2.4. NGGM predicted

For the projected accuracy of future ISR laser instruments, we consider the following spectra, which are predicted to be representative of the errors of these instruments at different years (p.c. Vitali Müller, Albert-Einstein-Institut, Hannover, March 2023):

$$s_{\mathrm{NGGM\ 2030},\rho}(f) = L_{\mathrm{ISR}}\frac{1\times10^{-15}}{f} + \frac{1\times10^{-13}}{f^2}\,\left[\frac{m}{\sqrt{Hz}}\right], \quad (10)$$

$$s_{\mathrm{NGGM\ 2033},\rho}(f) = L_{ISR}\frac{5\times10^{-16}}{f} + \frac{5\times10^{-14}}{f^2}\,\left[\frac{m}{\sqrt{Hz}}\right], \quad (11)$$

$$s_{\mathrm{NGGM\ 2040},\rho}(f) = L_{ISR}\frac{5\times10^{-17}}{f} + \frac{5\times10^{-15}}{f^2}\,\left[\frac{m}{\sqrt{Hz}}\right]. \quad (12)$$

The subscript indicates the year in which the instrument is predicted to be ready for flight. Refer to the teal, purple and yellow lines, respectively, in Fig. 4. We note that Eq. (10) is equivalent to Eq. (9), considering only thermal noise at low frequency (<1 mHz) and, therefore, no dependency on inter-satellite distance at low frequency. Eq. (11) is an improvement of factor 2 over Eq. (10), as already shown in GRACE-FO (Abich et al., 2019). Eq. (12) is one order of magnitude improvement, as expected by LISA (Dahl et al., 2019).

2.3. Accelerometry

2.3.1. Electrostatic accelerometry

As electrostatic accelerometers, we consider the goal requirements of the NGGM mission concept and the performance of the MicroSTAR accelerometer for the linear acceleration measurements. Fig. 6 presents an overview.

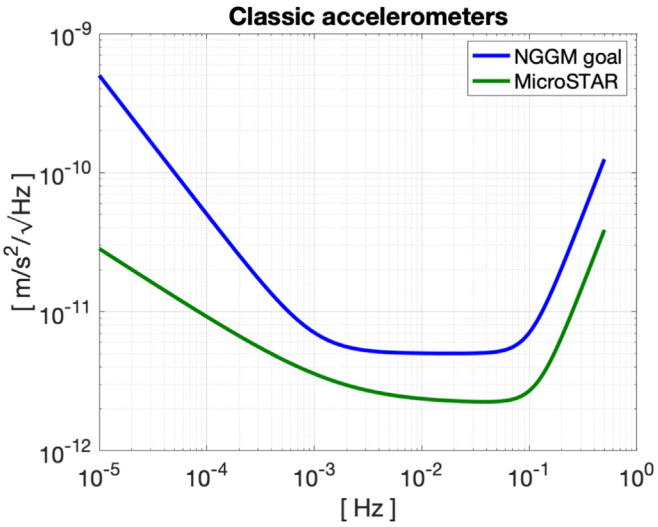

Fig. 6. Overview of the noise ASD of electrostatic accelerometers.

2.3.1.1. NGGM "goal" accelerometer. There are two requirements for the accelerometer performance of the NGGM mission concept: "goal" and "threshold" (Massotti et al., 2021). We selected the "goal" scenario with the associated noise ASD is defined by (cf. blue line in Fig. 6):

$$s_{\mathrm{NGGM,ng}}(f) = 5 \times 10^{-12} \times \sqrt{1 + (0.001/f)^2 + (100f^2)^2} \left[\frac{\mathrm{m}/s^2}{\sqrt{\mathrm{Hz}}}\right] \tag{13}$$

2.3.1.2. MicroSTAR. The MicroSTAR has a noise ASD given by the expression (Christophe et al., 2018), shown as the green line in Fig. 6:

$$s_{\mathrm{MicroSTAR,ng}}(f) = 2 \times 10^{-12} \times \sqrt{1.2 + 0.002f^{-1} + 6000f^4} \left[\frac{\mathrm{m}/s^2}{\sqrt{\mathrm{Hz}}}\right]. \tag{14}$$

2.3.2. Quantum accelerometry

We assume the following CAI scheme (Malossi et al., 2010):

i) a Bose-Einstein Condensate (BEC) atomic cloud is produced from a Magneto-Optical Trap (MOT) by laser cooling and magnetic trapping techniques,
ii) a Raman pulse splits the wave-packet in two, through the transfer of momentum with the photons, kicking them in opposite directions along the axis of the Raman lasers and over the interrogation period T,
iii) a second Raman pulse imparts opposite momentum to the wave-packet, forcing them to converge,
iv) after the same period of interrogation, a third Raman pulse recombines the wave-packet, and
v) the interferometric measurement is conducted using the recombined wave-packet.

We use the term *wave-packet* to recognise the wave-particle duality of the BEC because, formally, there is no physical separation of the atomic clouds. Only the wave function is spread in two directions. Henceforth, the term *(atom) cloud* intends to loosely refer to both the physical cloud (in the case of quantum gradiometry in Sections 2.4 and 4.2) and the wave-packet, except when it is essential to make a distinction. The first and third pulses are also called π/2 pulses, and the second pulse is called a π pulse.

A non-zero acceleration $\boldsymbol{a}$ along the axis of the Raman laser induces a phase shift ϕ proportional to the acceleration the atom clouds have experienced during $2T$ (Peters et al., 1999):

$$\phi = \boldsymbol{k}_{\mathrm{eff}} \cdot \boldsymbol{a}T^2. \tag{15}$$

The magnitude of the effective wavevector k_{eff} is inversely proportional to the wavelength of the Raman laser λ. In the case of the double-diffraction scheme considered in this study, as a result of the direct and reflected interactions with the Raman laser (Lévèque et al., 2009):

$$k_{\mathrm{eff}} = \frac{8\pi}{\lambda}. \tag{16}$$

By introducing the degree of entanglement α (e.g. for $\alpha = 0$, there is no entanglement and therefore reaching quantum projection noise; for$\alpha = 1$ the Heisenberg limit is attained), with interferometer contrast C and the number of atoms N, we expand the simple relation dependent only on the Signal-to-Noise Ratio (SNR), which is proportional to $\sqrt{N}$ (Sorrentino et al., 2010) to model the interferometric phase noise as:

$$s_{\Phi} = \frac{1}{\mathrm{C}N^{\frac{1+\alpha}{2}}}. \tag{17}$$

The interferometer contrast represents the intensity at which the interferometry fringes appear in the detector. The beam splitting efficiency and any external perturbations influence its value because they lead to a loss of atoms in the phase shift, mainly due to non-inertial effects. However, techniques exist to mitigate the rotation-induced loss of contrast (Kaczmarczuk et al., 2025). Experimental or assumed values range from 0.5 (Zahzam et al., 2022), 0.6 (Zhu et al., 2022) or 0.65 (Peters et al., 1999) to C = 0.8 (Knabe et al., 2022), while the maximum value is 1 (Douch et al., 2018) The degree of entanglement refers to various quantum enhancement techniques that enable the observation of phase differences after the interrogation time T with greater accuracy (Szigeti et al., 2021), with *Spin Squeezing* being the most common (Gross, 2012). Parameter α reflects the proportion of atoms in the cloud that are entangled, ranging from 0 to 1, where the value 0 means there is no entanglement. In the latter case, your error model is identical to Zahzam et al. (2022) and Zhu et al. (2022).

The momentum transfer δp is the product of the reduced Planck constant $\hbar$ with the magnitude of the wavevector k_{eff}:

$$\delta p = \hbar k_{\text{eff}} \tag{18}$$

For a single-axis instrument where the effective wavevector is aligned in the measured acceleration a, Eq. (15) can be written to accommodate the Momentum Space Separation β, which assumes integer values higher than one for multi-pulse (or "kicks") sequences:

$$\phi = \beta \frac{\delta p}{\hbar} a T^2. \tag{19}$$

Under these assumptions, the CAI accelerometer shot-to-shot (s2s) sensitivity, also called *quantum projection noise*, is:

$$s^{(s2s)}_{\text{CAI,ng}} = \frac{\hbar}{\beta \delta p T^2} s_\Phi = \frac{1}{\beta k_{\text{eff}} T^2 C N^{\frac{1+\alpha}{2}}} \tag{20}$$

We assume that the noise spectra of the CAI accelerometers are flat, corresponding to white noise (Sorrentino et al., 2014); for this reason, the standard deviation is sufficient to describe these errors entirely. This characteristic is the main advantage over classical accelerometers (Migliaccio et al., 2019), which are dominated by noise at low frequencies resulting from bias thermal fluctuations and gold wire damping (Reubelt et al., 2014; Christophe et al., 2015, 2018), with a characteristic $f^{-n}, n \geq 1$ frequency dependence.

2.3.2.1. Mode of operation. So far, we have limited our analysis to the shot-to-shot sensitivity of CAI, which represents the best-case scenario where measurements are made continuously without interruption. In reality, this is impossible because the atom cloud needs time to be prepared, which we assume to be $T_{\text{prep}} = 1s$ (Müntinga et al., 2013). Additionally, we define T_{cycle} as the complete measurement cycle period.

We identify two distinct modes for the design and operation of the CAI:

- *Concurrent* atom cloud preparation and interrogation, where the interferometry takes place at the same time as the BEC is being prepared: $T_{\text{cycle}} = T_{\text{prep}}$
- *Sequential* atom cloud preparation and interrogation, the process for cloud preparation and interrogation does not overlap, leading to a more extended measurement cycle period: $T_{\text{cycle}} = 2T + T_{\text{prep}}$.

In the concurrent case, the next atom cloud can be launched before the CAI sequence of the current atom cloud is completed, i.e., the measurement cycle T_{cycle} is only limited by the atom cloud preparation time T_{prep}, and we avoid any dead time between measurement cycles.

For both cases, the standard deviation of the CAI acceleration is:

$$s_{\text{CAI,ng}} = \sqrt{T_{\text{cycle}}} s^{(s2s)}_{\text{CAI,ng}}. \tag{21}$$

Additional considerations regarding how the Coriolis accelerations influence both operation modes are discussed in Section 5.1.

One consequence of the two operational modes is the cloud velocity, which is analysed in Section 5.1. The sequential mode of operation allows for an initial zero-atom cloud velocity, as the preparation of the BEC and interferometric chambers is performed at the same location. The BEC is directly prepared at the CoM, and the wave packet propagates exclusively along the axis of the Raman laser (left of Fig. 7), with momentum depicted by the blue arrows, resulting from the momentum transfer imparted by the Raman laser alone Zahzam et al., 2022. For the concurrent mode of operation, the atom cloud enters one side of the chamber with a non-zero (physical) velocity perpendicular to the Raman laser (green arrow in Fig. 7), for example, $v_{\text{cloud}} = 2.5\,\text{cm/s}$ (Carraz et al., 2014; Trimeche et al., 2019). An additional recoil laser with its axis perpendicular to that of the Raman laser, imparts a transverse velocity v_{cloud} to the atom cloud. The first $\pi/2$ pulse is done on one side of the chamber by the first Raman laser, the π pulse is done by a second Raman laser in the middle of the chamber, and the third Raman laser on the opposite side of the chamber is responsible for the second $\pi/2$ pulse.

For both operation models, the mirror(s) tilt to compensate for the satellite rotation, i.e., they rotate between the laser pulses of the CAI. The concurrent mode requires three mirrors in different locations along the direction of the atom's movement.

2.3.3. Selection of CAI parameters

To guide our selection of future CAI instrument parameters, we selected a set of representative instrument configurations based on a simplified performance model, Eqs. (85) and (86), and heuristic cost proxies, Table 5 (cf. Appendix 8.7). This model serves as a practical link between achievable performance and feasible instrument design. The selected configurations are not intended as optimal designs, but as reasonable inputs for further assessment within our study. These predictions serve as the basis for deriving a cost metric based on mass, volume, complexity, and program risk, allowing us to identify parameter combinations that offer plausible instrument sensitivity while remaining technically viable. If this trade-off is not done, the instrument sensitivity can be arbitrarily chosen.

Fig. 8 illustrates the resulting parameter space, showing how instrument sensitivity varies against the qualitative cost metric aiming. The selected configurations are not

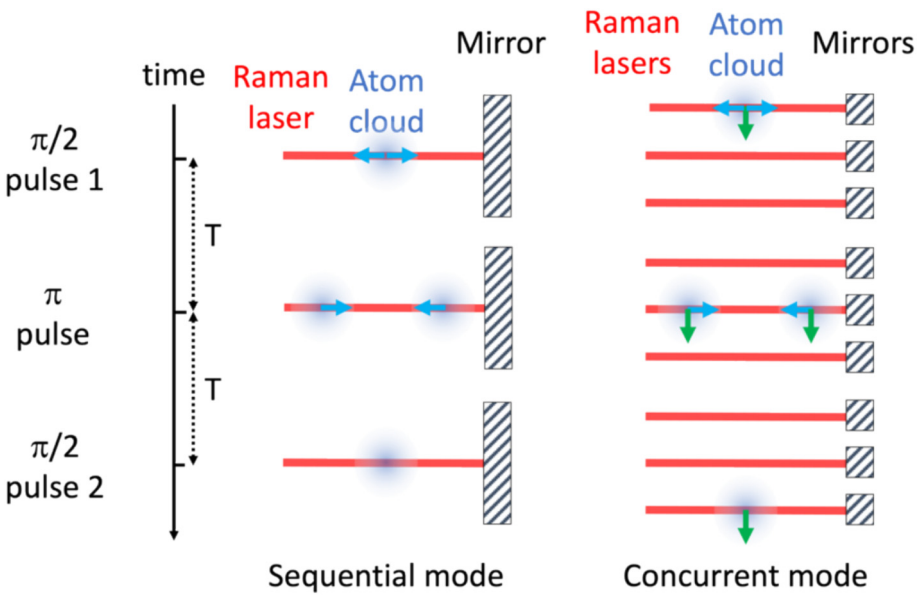

Fig. 7. Diagram of the interferometry scheme for the sequential (left) and concurrent modes (right), showing the wave-packets (blue *atom cloud*) after the respective Raman laser pulses, which add momentum as represented by the blue arrows. In the case of the concurrent mode (right), the transverse (physical) velocity represented by the green arrow is provided at the start of the measurement sequence by an additional laser (not shown) perpendicular to the Raman lasers.

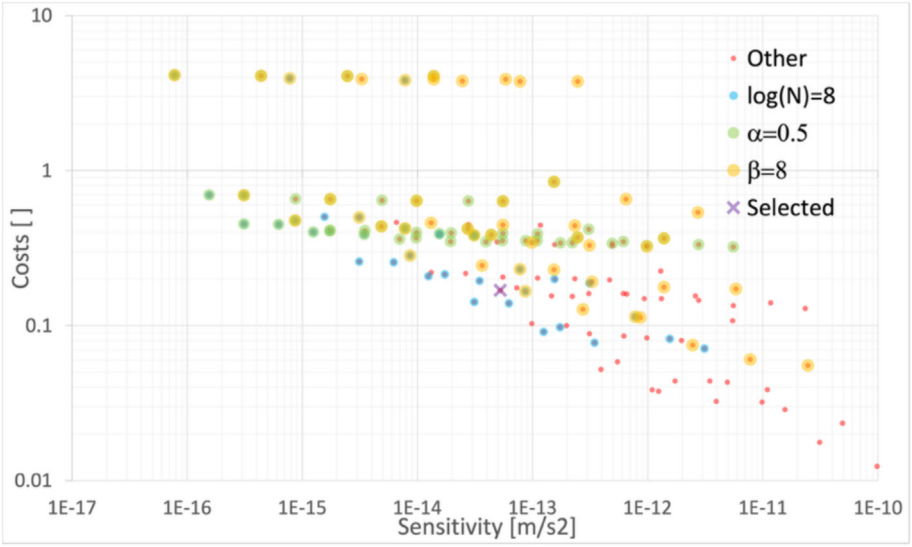

Fig. 8. Trade Space Exploration, highlighting those options with extreme values for the CAI parameters (cyan, green and yellow) and the selection shown in Table 2 (purple cross).

intended as optimal designs, but as reasonable inputs for further assessment within the broader study. Additional details of this analysis are shown in Appendix 8.7.

2.4. Gradiometry

In both classical and quantum GG, we consider this technique to be implemented by combining pairs of accelerometers. As such, the error spectra of the electrostatic and quantum accelerometers can be directly converted to gradiometer measurements by dividing the former by the length of the gradiometer arm L_{GG}, which is the distance between pairs of accelerometers on the same axis. Therefore, considering the MicroSTAR accelerometer (Section 2.3.1.2), with a noise floor of 2×10^{-12} m/s^2, a gradiometer built with these instruments with $L_{GG} = 0.5$m would have a noise floor of 4×10^{-12}s^{-2} or 4mE.

The motivation for including a gradiometer in this study is to establish the requirements for a CAI gradiometer, considering that electrostatic accelerometers are unable to attain the necessary accuracy, as depicted in Fig. 9. In this figure, the gravity gradient signal in the radial direction due

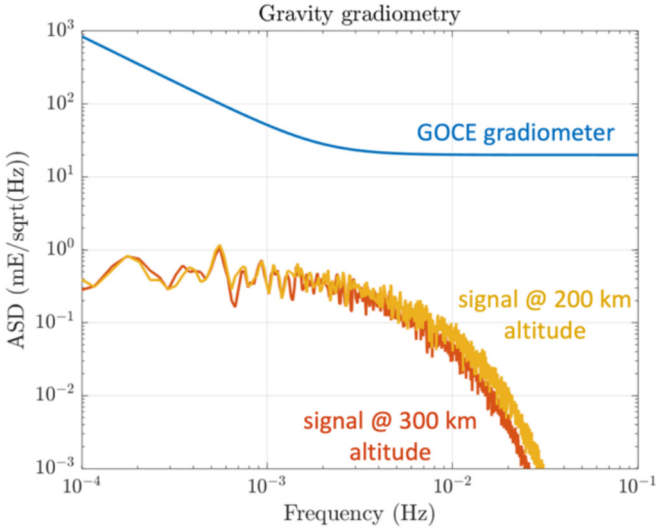

Fig. 9. Comparison between the GOCE gradiometer errors (blue line) with the time-variable signal in terms of gravity gradient at 200 km (yellow line) and 300 km altitudes (red lines).

to the time-variable gravity field, i.e. excluding the mean gravity field, at altitudes of 200 km and 300 km is shown in the yellow and red lines, respectively; the noise of GOCE gravity gradients is shown for reference in the blue line. Sub-mE gradiometry is required, which necessitates an electrostatic instrument that is at least one order of magnitude more accurate than the MicroSTAR accelerometer operating under ideal conditions.

For quantum gradiometry, the measurement concept is similar to quantum accelerometry (Section 2.3.2), except that it is doubled along the axis where the gravity gradient is measured. The original atom cloud is physically split in two with a high-recoil laser pulse, resulting in two CAI accelerometers. Differential acceleration is therefore measured between the 2 CAI accelerometers. Common acceleration is then rejected as the 2 CAI share the same Raman laser pulses, and the gravity gradient along the Raman axis remains. This scheme applies to both sequential and concurrent modes of operation, with the obvious difference that the atom clouds are not moving perpendicularly to the Raman laser in the first mode. The amplitude of the gravity gradient as a function of the differential phase measurement and associated errors is closely related to ϕ in Eq. (15) and $s_{\mathrm{CAI,ng}}$ in Eq. (21), as discussed in Section 4.2.

3. Low-low satellite to satellite tracking

The ll-SST concept relies on precise ranging between two satellites flying in the same low-altitude orbit, separated by a certain distance along the orbit (220 km in the case of the GRACE and GRACE-FO missions). In a variant of this concept, labelled cross-track ll-SST, the along-track distance is kept minimal, and the second orbit has a different right ascension of the ascending node than the first orbit to achieve ranging predominantly in the cross-track acceleration, away from the poles. The cross-track ll-SST must maintain a minimum along-track separation for collision avoidance at the poles, where the orbits cross each other. In all ll-SST cases, the changes in the ISR are caused by variations in gravity and non-gravitational forces. Therefore, the concept foresees accelerometers measuring non-gravitational accelerations, allowing the signal due to gravity to be extracted from the ranging measurements or driving a drag compensation system, similar to GOCE.

In the following, vector equations are transformed into their components using the indices i, j, and k for the coordinate axes x, y, and z, respectively. Their relation is as arbitrary as the definition of the reference frames. For example, we may define $i,j,k \equiv x,y,z$ for along-track ll-SST and $i,j,k \equiv y,z,x$ for cross-track ll-SST, assuming the traditional axis nomenclature where x is aligned with the along-track direction, y with the cross-track direction, and z with the radial direction, in a circular low-Earth orbit (LEO) orbit.

3.1. ll-SST with electrostatic accelerometers

The proposed ll-SST concept is illustrated in Fig. 10. The ISR system is similar to GRACE-FO's LRI, which is implemented in the so-called racetrack configuration with a Triple Mirror Assembly (TMA). This concept has the benefit that the ISR is performed between the satellites' CoM without physically occupying those locations while not compromising the ranging performance (Sheard et al., 2012).

In the case of electrostatic instrumentation, the accelerometer measurements will be affected by imperfections such as scale factors and biases (Touboul et al., 2016). To achieve the accelerometer accuracy defined by the noise ASD, these imperfections must be corrected. While the biases can be estimated via precise orbit determination (Helleputte et al., 2009; Visser and IJssel, 2016), the scale factors of accelerometers placed symmetrically around the satellite's CoM can be accurately calibrated using other instruments that observe the satellite rotation, e.g., star sensors and gyroscopes, and a gravity field model (Siemes et al., 2019). Therefore, we foresee two accelerometers, labelled ACC 1 and ACC 2, symmetrically placed around the satellite CoM, which facilitates an accurate calibration of the accelerometers that would not be possible in the case of a single accelerometer placed at the satellite's CoM. We assume that the two accelerometers are at a nominal distance of $L_{\mathrm{acc}} = 0.5$ m from each other.

The LTI is equipped with a DWS sensor that measures the direction of the incoming laser beam. Combined with accurate knowledge of the satellite positions from GNSS, this allows for deriving the attitude of the satellites relative to the LOS vector (Section 2.1.3.2). Obviously, this provides pitch and yaw, but not the roll about the LOS. The attitude is also observed by star trackers (Section 2.1.1),

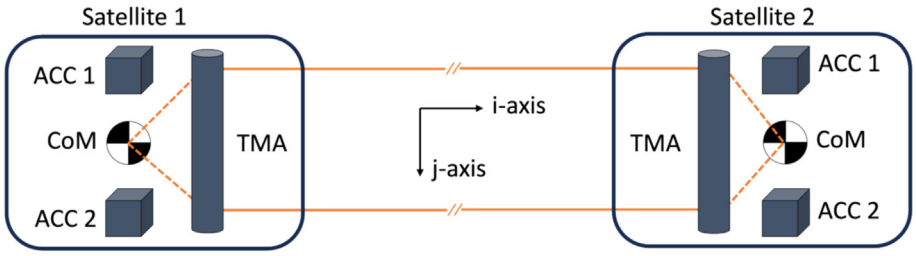

Fig. 10. Diagram of the assumed concept for ll-SST with electrostatic accelerometers.

augmented by the accelerometers (Section 2.1.4), and optionally, a high-performance IMU (Section 2.1.2).

To extract the non-gravitational acceleration from the accelerometer measurements, we form the so-called common-mode acceleration (Massotti et al., 2021). The common mode acceleration along the generic axis i is:

$$a_{\mathrm{ng},i} = \frac{a_{1i} + a_{2i}}{2}, \tag{22}$$

where $i \equiv x$ is for the along-track ISR, and $i \equiv y$ is for the cross-track ISR. Through error propagation, we obtain the noise spectrum of a_{ng} to be $\sqrt{2}$ smaller than the linear acceleration error measured by a single accelerometer $s_{\mathrm{acc,ng}}(f)$ (Section 2.3.1):

$$s^2_{\mathrm{ng}}(f) = \frac{1}{2} s^2_{\mathrm{acc,ng}}(f). \tag{23}$$

The inter-satellite range acceleration $\ddot{\rho}$ contains the effects of both gravitational and non-gravitational accelerations acting on the two satellites, as well as the centrifugal acceleration of the LOS baseline (since this vector is rotating in inertial space). The non-gravitational accelerations are removed by subtracting the common-mode accelerations, assuming that the i-axis is aligned with the LTI axis. The centrifugal acceleration is a function of the ISR ρ and the inertial radial and cross-track velocities, v_z and v_y respectively, assuming a nominal local horizontal attitude of the inter-satellite vector:

$$\ddot{\rho}_{\mathrm{grav}} = \ddot{\rho} - \frac{1}{\rho}\left(v_y^2 + v_z^2\right) - a^{(1)}_{\mathrm{ng},i} + a^{(2)}_{\mathrm{ng},i}. \tag{24}$$

Error propagation gives the noise spectrum of $\ddot{\rho}_{\mathrm{grav}}$ as a function of σ_{ng}, the ISR error σ_{ISR} (Section 2.2) and errors in reconstructing the centrifugal accelerations s_c:

$$s^2_{\ddot{\rho}}(f) = s^2_{\mathrm{ISR}}(f) + s^2_{\mathrm{c}}(f) + 2s^2_{\mathrm{ng}}(f) \tag{25}$$

We will not further consider the errors in reconstructing the centrifugal accelerations s_c because several studies, e.g., Weigelt (2017) and Ghobadi-Far et al. (2018) have demonstrated that these errors are limited to low frequencies and using the variational equation approach for gravity field estimation effectively suppresses them. Nevertheless, for completeness, this error term is quantified for GRACE-FO in Appendix 8.6.

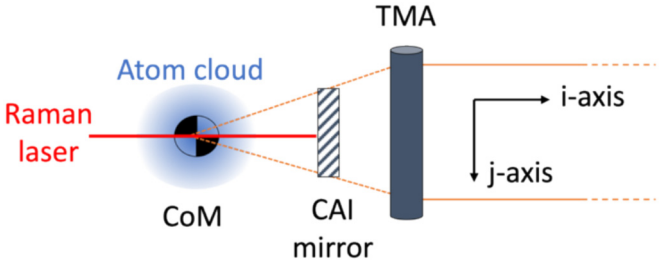

Fig. 11. Diagram of the assumed concept of ll-SST with quantum accelerometers. Only one satellite is shown.

3.2. ll-SST with quantum accelerometers

The ll-SST concept is limited by the performance of the electrostatic accelerometers at longer wavelengths, specifically frequencies near and below the orbital period (Cheng and Ries, 2017), which motivates replacing them with quantum accelerometers to eliminate this limitation (Travagnin, 2020). Unlike electrostatic accelerometers, quantum ones do not require calibration. Therefore, it is sufficient to place one quantum accelerometer into the satellite CoM, as shown in Fig. 11, which has the benefit that the accelerometer directly measures the non-gravitational acceleration and is insensitive to centrifugal and Euler forces and gravity gradients. However, depending on the operational mode (Section 2.3.2.1), the atom cloud may be in motion during the interferometric measurement process, and we must account for the effects of the Coriolis force (Section 3.2.1).

The quantum accelerometer measures the phase Φ of the CAI, which is proportional to the acceleration of the atom cloud $\boldsymbol{a}_{\mathrm{cloud}}$ relative to the acceleration of the mirror that reflects the laser $\boldsymbol{a}_{\mathrm{mirror}}$, the momentum (vector) transfer $d\boldsymbol{p}$ and the square of interrogation time T between laser pulses:

$$\Phi = \frac{d\boldsymbol{p}}{\hbar} \cdot (\boldsymbol{a}_{\mathrm{cloud}} - \boldsymbol{a}_{\mathrm{mirror}}) T^2, \tag{26}$$

where $d\boldsymbol{p}$ is the momentum (vector) transfer that defines the direction in which the acceleration is sensed, and its magnitude is given by Eq. (18).

Since the mirror is firmly attached to the satellite, unlike the atom cloud, it serves as a reference for the

non-gravitational accelerations $\boldsymbol{a}_{\mathrm{ng}}$ experienced by the satellite so that:

$$\boldsymbol{a}_{\mathrm{mirror}} = \boldsymbol{a}_{\mathrm{ng}}. \tag{27}$$

In contrast, the atom cloud freely floated in inertial space during the interrogation time. The acceleration of the atom cloud can be expressed as:

$$\boldsymbol{a}_{\mathrm{cloud}} = -\left(\boldsymbol{V} - \Omega^2 - \dot{\Omega}\right)\left(\boldsymbol{r}_{\mathrm{cloud}} - \boldsymbol{r}_{\mathrm{CoM}}\right) + 2\boldsymbol{\omega} \times \boldsymbol{v}_{\mathrm{cloud}}, \tag{28}$$

with the gravity gradient tensor as:

$$\boldsymbol{V} = \begin{bmatrix} V_{ii} & V_{ij} & V_{ik} \\ V_{ij} & V_{jj} & V_{jk} \\ V_{ik} & V_{jk} & V_{kk} \end{bmatrix}, \tag{29}$$

the angular velocity vector is:

$$\boldsymbol{\omega} = \begin{bmatrix} \omega_i \\ \omega_j \\ \omega_k \end{bmatrix},$$

the angular rate tensor is:

$$\Omega = \begin{bmatrix} 0 & -\omega_k & \omega_j \\ \omega_k & 0 & -\omega_i \\ -\omega_j & \omega_i & 0 \end{bmatrix} \text{ and}$$

$$\Omega^2 = \begin{bmatrix} -\omega_j^2 - \omega_k^2 & \omega_i\omega_j & \omega_i\omega_k \\ \omega_i\omega_j & -\omega_k^2 - \omega_i^2 & \omega_j\omega_k \\ \omega_i\omega_k & \omega_j\omega_k & -\omega_i^2 - \omega_j^2 \end{bmatrix} \tag{30}$$

and the angular acceleration as:

$$\dot{\Omega} = \begin{bmatrix} 0 & -\dot{\omega}_k & \dot{\omega}_j \\ \dot{\omega}_k & 0 & -\dot{\omega}_i \\ -\dot{\omega}_j & \dot{\omega}_i & 0 \end{bmatrix}. \tag{31}$$

The remaining symbols are the position of the atom cloud $\boldsymbol{r}_{\mathrm{cloud}}$, the position of the satellite CoM $\boldsymbol{r}_{\mathrm{CoM}}$, and the velocity of the atom cloud $\boldsymbol{v}_{\mathrm{cloud}}$ relative to the satellite CoM. The term $\dot{\Omega}$ represents the angular acceleration matrix which causes Euler accelerations, Ω^2 causes the centrifugal accelerations, and $2\boldsymbol{\omega} \times \boldsymbol{v}_{\mathrm{cloud}}$ is the Coriolis acceleration.

Combining the above, we obtain the measured acceleration along the direction defined by the Raman laser axis, represented by the unit vector $\boldsymbol{e}_i = d\boldsymbol{p}/dp$, as:

$$\boldsymbol{e}_i \cdot \boldsymbol{a}_{\mathrm{ng}} = \\ = -\frac{\hbar}{dpT^2}\Phi + \boldsymbol{e}_i \cdot \left(-\left(\boldsymbol{V} - \Omega^2 - \dot{\Omega}\right)\left(\boldsymbol{r}_{\mathrm{cloud}} - \boldsymbol{r}_{\mathrm{CoM}}\right) + 2\boldsymbol{\omega} \times \boldsymbol{v}_{\mathrm{cloud}}\right). \tag{32}$$

The derivation of the equation above is presented in Section 8.1.1.

Since we measure the acceleration in the direction of the momentum transfer $d\boldsymbol{p}$, this vector must be aligned with the laser used for measuring the ISR. Furthermore, we disregard any effects of magnetic fields and self-gravity on the atom cloud, which may play a role, given the extreme sensitivity of the quantum sensor. These considerations are beyond the scope of this study because they heavily depend on the specific instrument and satellite design.

If the atom cloud is in the satellite CoM, i.e., $\boldsymbol{r}_{\mathrm{cloud}} - \boldsymbol{r}_{\mathrm{CoM}} = 0$, the equation above simplifies to:

$$\boldsymbol{e}_i \cdot \boldsymbol{a}_{\mathrm{ng}} = -\frac{\hbar}{dpT^2}\Phi + \boldsymbol{e}_i \cdot \left(2\boldsymbol{\omega} \times \boldsymbol{v}_{\mathrm{cloud}}\right), \tag{33}$$

leaving the Coriolis term as the only effect to consider. In this context, we note that $\boldsymbol{r}_{\mathrm{cloud}} - \boldsymbol{r}_{\mathrm{CoM}} = 0$ holds for the initial position of the atom cloud. The first laser pulse of the CAI splits the wave-packet into two that move at a similar speed in opposite directions along the laser axis, away from the initial position, as indicated in step ii of Section 2.3.2. We assume that the rate of rotation of the Raman laser, i.e., the rotation of the satellite after the compensation by the tilting mirror, does not change significantly during the outward and inward wave-packet drift, indicated as steps ii to iv in Section 2.3.2. Under these conditions, the integrated effect of the rotational and gravity gradient terms cancel out over the outward and inward momentum changes of the two wave-packets and are negligible at their recombination. The impact of the inhomogeneous velocity profile across the atom cloud can also be neglected (Beaufils et al., 2023).

Considering axis i, j, and k are arbitrary, e.g., $i, j, k \equiv x, y, z$ for along-track ll-SST and $i, j, k \equiv y, z, x$ for cross-track ll-SST, we can express the equation in scalar form as:

$$a_{\mathrm{ng},i} = -\frac{\hbar}{dpT^2}\Phi + 2\omega_j v_{\mathrm{cloud},k} - 2\omega_k v_{\mathrm{cloud},j}. \tag{34}$$

3.2.1. Error amplitude of quantum accelerometers

Considering the error in the atom cloud velocity knowledge $\sigma_{v,\mathrm{cloud}}$, angular rate error σ_ω after compensation by the tilting mirror, and applying error propagation (and considering the effect of the discrete CAI measurement cycle period T_{cycle}), we obtain:

$$s^2_{a_{\mathrm{ng},i}} = \frac{T_{\mathrm{cycle}}}{T^4}\frac{s^2_\Phi}{\beta^2 k^2_{\mathrm{eff}}} + \\ + 4\omega_j^2 s^2_{v,\mathrm{cloud},k} + 4\omega_k^2 s^2_{v,\mathrm{cloud},j} + 4s^2_{\omega,j} v^2_{\mathrm{cloud},k} + 4s^2_{\omega,k} v^2_{\mathrm{cloud},j}. \tag{35}$$

We can group the first term as the CAI acceleration sensitivity error $\sigma_{\mathrm{CAI,ng}}$ (cf. Section 2.3.2) and the last four terms as the errors $s_{\mathrm{Cor},i}$ caused by the Coriolis effect:

$$s^2_{a_{\mathrm{ng},i}} \equiv s^2_{\mathrm{CAI,ng},i} + s^2_{\mathrm{Cor},i}. \tag{36}$$

3.3. Cloud velocity

The equation of the variance of the Coriolis term depends on the velocity of the atom cloud and the angular velocity of the Raman laser, cf. Eq. (35). In this section, we analyse the individual contributions in more detail and explain the underlying assumptions on signals and errors.

The atom cloud velocity components that contribute to the variance of the Coriolis term are perpendicular to the Raman laser axis, since we assume that their integrated effects associated with the outwards and inwards momentum changes of the cloud along the Raman laser axis are negligible.

Since no instrument is perfect, the atom cloud has a random, non-zero velocity when released from the Magneto-Optical Trap (MOT). We assume the worst-case value of the initial cloud velocity to be $s_{v_{\text{cloud,initial}}} = 10^{-7}\text{m/s}$. It should be noted that treating this worst-case value as an error is a conservative estimate if a technique called Delta Kick-Collimation (DKC) is used (Amri, 2022).

The thermal velocity (most probable speed) of individual atoms is:

$$v_{\text{atom, therm}} = \sqrt{\frac{2k_B T_{\text{atom}}}{m}}, \tag{37}$$

where k_B is the Stefan Boltzmann constant, T_{atom} is the atom temperature, and m is the atom mass. In practice, $v_{\text{atom,therm}}$ tends to be at the order of 10^{-4}m/s, but DKC allows for values at the micrometre per second (Amri, 2022). For this reason, we assume that $v_{\text{atom,therm}} = 10^{-6}\text{m/s}$.

Recalling that the velocity dispersion follows the Maxwell-Boltzmann distribution (Amri, 2022), we are interested in the difference between the most probable speed $v_{\text{atom,therm}}$ and the velocity Root Mean Square (RMS), which is given by $\sqrt{3/2}v_{\text{atom,therm}}$. Under this assumption, the thermal velocity of the atom cloud is:

$$s_{v_{\text{cloud,therm}}} = \frac{\left(\sqrt{\frac{3}{2}} - 1\right) v_{\text{atom, therm}}}{\sqrt{N}}, \tag{38}$$

due to the averaging over N atoms. Thus, assuming that $s_{v_{\text{cloud,initial}}}$ is uncorrelated to $s_{v_{\text{cloud,therm}}}$, the variability of the atom cloud velocity is:

$$s^2_{v_{\text{cloud}}} = s^2_{v_{\text{cloud,therm}}} + s^2_{v_{\text{cloud,initial}}}. \tag{39}$$

3.4. Effect of attitude uncertainty in ll-SST

So far, we have derived the noise spectra for the observations in the satellite reference frame (SRF). However, the observations need to be transformed to the Earth-centred, Earth-fixed (ECEF) reference frame. The transformation requires satellite attitude data and, therefore, is not error-free. In this section, we analyse the impact of attitude errors.

The effects of attitude uncertainty discussed in this section are conceptually separate from other attitude errors discussed so far, notably the Coriolis effect on CAI accelerometers.

Conceptually, we need to subtract the ISR acceleration $\ddot{\rho}_{ng}$ due to non-gravitational accelerations from the measured ISR acceleration $\ddot{\rho}$ to obtain $\ddot{\rho}_{\text{grav}}$ due to gravitational accelerations:

$$\ddot{\rho}_{\text{grav}} = \ddot{\rho} - \frac{1}{\rho}\left(v_y^2 + v_z^2\right) - \ddot{\rho}_{\text{ng}}. \tag{40}$$

For this analysis, we isolate the term $\ddot{\rho}_{\text{ng}}$, i.e., the differential non-gravitational acceleration projected onto the LOS connecting the two satellites' centres of mass, i.e.:

$$\ddot{\rho}_{\text{ng}} = \left(\boldsymbol{a}^{(}_{\text{ng}}1) - \boldsymbol{a}^{(}_{\text{ng}}2)\right) \cdot \boldsymbol{e}_{\text{LOS}} = \Delta\boldsymbol{a}_{\text{ng}} \cdot \boldsymbol{e}_{\text{LOS}}, \tag{41}$$

where $\boldsymbol{e}_{LOS}$ is the LOS unit, which is defined by the satellite positions, and is naturally provided in the Earth-centred, inertial (ECI) frame.

$$\boldsymbol{e}_{\text{LOS}} = \frac{\boldsymbol{r}^{(1)} - \boldsymbol{r}^{(2)}}{\|\boldsymbol{r}^{(1)} - \boldsymbol{r}^{(2)}\|}. \tag{42}$$

If $\boldsymbol{r}^{(1)}$ or $\boldsymbol{r}^{(2)}$ are provided in the ECEF frame, we assume that the necessary coordinate transformation to the Earth-centred, inertial (ECI) reference frame does not introduce a significant error because the Earth Orientation Parameters are well known. As for the non-gravitational accelerations of satellite 1 and satellite 2, $\boldsymbol{a}^{(}_{\text{ng}}1)$ and $\boldsymbol{a}^{(}_{ng}2)$, respectively, they are defined in the ECI reference frame in Eq. (41) but measured in the SRF, which we represent as $\boldsymbol{a}^{(\text{SRF},l)}_{\text{ng}}$ for satellite l. Therefore, we need to perform a coordinate transformation for the accelerations, based on the satellite attitude data, from the SRF to the ECI frame, which can be represented as

$$\boldsymbol{a}^{(}_{\text{ng}}\text{ECI},l) = \boldsymbol{R}^{(}\text{ECI[LFTARW]SRF},l)\boldsymbol{a}^{(\text{SRF},l)}_{\text{ng}}. \tag{43}$$

The SRF-to-ECI rotation matrix contains errors, here represented by the small angle rotation matrix $\Theta^{(}\text{ECI[LFTARW]SRF},\text{s})$:

$$\begin{aligned}&\boldsymbol{R}^{(}\text{ECI[LFTARW]SRF},l)\\ &= \boldsymbol{R}^{(}\text{ECI[LFTARW]SRF},l,\text{true})\Theta^{(}\text{ECI[LFTARW]SRF},l).\end{aligned} \tag{44}$$

We split $\Theta^{(}\text{ECI[LFTARW]SRF},l)$ into the identity matrix and the small angle rotations, given as Euler angles errors $\theta_{\text{roll,l}}$, $\theta_{\text{pitch,l}}$ and $\theta_{\text{yaw,l}}$ for satellite l:

$$\begin{aligned}&\Theta^{(}\text{ECI[LFTARW]SRF},l)\\ &= \boldsymbol{E}^{(l)} + \boldsymbol{I} = \begin{bmatrix} 0 & -\theta_{\text{yaw,l}} & \theta_{\text{pitch,l}} \\ \theta_{\text{yaw,l}} & 0 & -\theta_{\text{roll,l}} \\ -\theta_{\text{pitch,l}} & \theta_{\text{roll,l}} & 0 \end{bmatrix} + \boldsymbol{I}.\end{aligned} \tag{45}$$

With these definitions, we can write:

$$\boldsymbol{a}^{(\text{ECI},l)}_{\text{ng}} = \boldsymbol{a}^{(\text{ECI,true},l)}_{\text{ng}} + \boldsymbol{E}^{(l)}\boldsymbol{a}^{(\text{SRF},l)}_{\text{ng}}, \tag{46}$$

where the only term on the right-hand side that is not perfectly known (for this analysis) is $\boldsymbol{E}^{(l)}\boldsymbol{a}^{(\text{SRF},l)}_{\text{ng}}$. Replacing in Eq. (41):

$$\ddot{\rho}^{(ECI)}_{\text{ng}} = \left(\Delta\boldsymbol{a}^{(\text{ECI,true})}_{\text{ng}} + \left(\boldsymbol{E}^{(1)} - \boldsymbol{E}^{(2)}\right)\Delta\boldsymbol{a}^{(\text{SRF})}_{\text{ng}}\right) \cdot \boldsymbol{e}^{(}_{\text{LOS}}\text{ECI}), \tag{47}$$

Assuming the attitude errors of $\boldsymbol{E}^{(I)}$, represented by the vector $\boldsymbol{s}_\theta$, are the same for both satellites, the error propagation of Eq. (47) is

$$s^{(ECI)}_{\ddot{\rho}_{\mathrm{ng}},\theta} = \nabla\ddot{\rho}^{(ECI)}_{\mathrm{ng}}[s_\theta]\nabla\ddot{\rho}^{(ECI)^T}_{\mathrm{ng}}, \tag{48}$$

with the Jacobian $\nabla = \left[\frac{\partial}{\partial\theta_{\mathrm{roll}}}\ \frac{\partial}{\partial\theta_{\mathrm{pitch}}}\ \frac{\partial}{\partial\theta_{\mathrm{yaw}}}\right]$ and $[s_\theta]$ the diagonal matrix with the errors of θ_{roll}, θ_{pitch} and θ_{yaw}, i.e., $s_{\theta_{\mathrm{roll}}}$, $s_{\theta_{\mathrm{pitch}}}$, and $s_{\theta_{\mathrm{yaw}}}$.

Evaluating Eq. (48), we arrive at the ranging error due to attitude $s_{\ddot{\rho}_{\mathrm{ng}},\theta}$ as a function of $\boldsymbol{s}_\theta = \left[s_{\theta_{\mathrm{roll}}} s_{\theta_{\mathrm{pitch}}} s_{\theta_{\mathrm{yaw}}}\right]^{\mathrm{T}}$:

$$s^{(ECI)}_{\ddot{\rho}_{\mathrm{ng}},\theta} = \sqrt{2}\begin{bmatrix} \Delta a^{(\mathrm{SRF})}_{\mathrm{ng,y}} e^{(}_{\mathrm{LOS,z}}\mathrm{ECI}) - \Delta a^{(\mathrm{SRF})}_{\mathrm{ng,z}} e^{(}_{\mathrm{LOS,y}}\mathrm{ECI}) \\ \Delta a^{(\mathrm{SRF})}_{\mathrm{ng,x}} e^{(}_{\mathrm{LOS,z}}\mathrm{ECI}) - \Delta a^{(\mathrm{SRF})}_{\mathrm{ng,z}} e^{(}_{\mathrm{LOS,x}}\mathrm{ECI}) \\ \Delta a^{(\mathrm{SRF})}_{\mathrm{ng,x}} e^{(}_{\mathrm{LOS,y}}\mathrm{ECI}) - \Delta a^{(\mathrm{SRF})}_{\mathrm{ng,y}} e^{(}_{\mathrm{LOS,x}}\mathrm{ECI}) \end{bmatrix}^{\mathrm{T}} \boldsymbol{s}_\theta. \tag{49}$$

We make the conservative assumption that the amplitude of $\Delta\boldsymbol{a}^{(\mathrm{SRF})}_{\mathrm{ng}}$ is given by the RMS of the non-gravitational accelerations at orbital altitude and take the component with the largest magnitude in each entry of the row vector in Eq. (49). We further assume that the amplitude of $\boldsymbol{e}^{(}_{\mathrm{LOS}}\mathrm{ECI})$ is 1 and drop the superscript of the reference frame because the errors have the same amplitude in any frame. Eq. (49) simplifies to

$$\rho_{\ddot{\rho}_{\mathrm{ng}},\theta} = \sqrt{2}\begin{bmatrix} \max\left(\mathrm{RMS}\left(a_{\mathrm{ng,z}}\right), \mathrm{RMS}\left(a_{\mathrm{ng,z}}\right)\right) \\ \max\left(\mathrm{RMS}\left(a_{\mathrm{ng,x}}\right), \mathrm{RMS}\left(a_{\mathrm{ng,z}}\right)\right) \\ \max\left(\mathrm{RMS}\left(a_{\mathrm{ng,x}}\right), \mathrm{RMS}\left(a_{\mathrm{ng,y}}\right)\right) \end{bmatrix}^{\mathrm{T}} \boldsymbol{s}_\theta. \tag{50}$$

In the case of homogeneous attitude error, $s_{\theta_{\mathrm{yaw}}} = s_{\theta_{\mathrm{pitch}}} = s_{\theta_{\mathrm{roll}}} \equiv s_\theta$, for example, if there are multiple star tracker cameras and their data is combined optimally with additional attitude sensors, such as an IMU and DWS:

$$s_{\ddot{\rho}_{\mathrm{ng}},\theta} = \sqrt{2}\mathrm{RMS}\left(a_{\mathrm{ng,x}}\right)s_\theta. \tag{51}$$

The values for $\mathrm{RMS}\left(a_{\mathrm{ng,x}}\right)$, $\mathrm{RMS}\left(a_{\mathrm{ng,y}}\right)$ and $\mathrm{RMS}\left(a_{\mathrm{ng,z}}\right)$ we considered in this study are presented in Appendix 8.3 and are functions of the Drag-Free Control (DFC) system. We quantify the effect of these errors in Section 5.2 for both electrostatic and quantum accelerometry.

4. Gradiometry

One important distinction between classical and short-term quantum gradiometry is that in the former case, the accelerometers are sensitive to all directions. This results in the possibility of measuring off-diagonal gravity gradient components, even with a single gradiometer arm. There are theoretical studies on vector quantum accelerometers (Barrett et al., 2019) but we assume this technology will be unavailable in the near future due to its inherent complexities and engineering challenges in obtaining an off-diagonal gravity gradient with high common rejection. For example, a single diagonal gravity gradient instrument has been evaluated to have a Size, Weight, and Power (SWAP) of approximately 1000 mm × 750 × 800 mm, 250 kg, 850 W in (Trimeche et al., 2019). In the case of quantum gravimetry, the CAI instruments we consider are inherently unidirectional and only sensitive to the gravity gradient along the axis connecting the atom clouds. Three CAI gradiometer instruments installed perpendicular to each other in the same satellite are needed to retrieve all diagonal terms of the gravity gradient tensor. For simplicity, we assume this to be the case without delving into the engineering aspects of this configuration. For more information on the configuration, the reader is invited to read Trimeche et al. (2019).

4.1. Gradiometry with electrostatic accelerometers

The GOCE mission demonstrated GG based on electrostatic accelerometers. The configuration of accelerometers is illustrated in Fig. 12. Here, we assume the same concept but with more advanced accelerometers and, potentially, a high-performance gyroscope. For reference, we take a distance of $L_{\mathrm{GG}} = 0.5\mathrm{m}$ between the accelerometers located on the same axis.

4.1.1. Error amplitude of classical gradiometers

The diagonal element V_{ii} of the gravity gradient tensor, measured by the accelerometer pair 1 and 4, is calculated with (Rummel et al., 2011):

$$V_{ii} = -\frac{a_{1,i} - a_{4,i}}{L_{\mathrm{GG}}} - \omega_j^2 - \omega_k^2. \tag{52}$$

For the remaining diagonal elements V_{jj} and V_{kk}, the expressions are similar to those for pairs 2,5 and 3,6, respectively, and for angular velocity components *i,k,* and *i,j*, respectively. After error propagation, there are non-linear terms that result in the product of angular velocity and angular velocity noise components, following approximations such as:

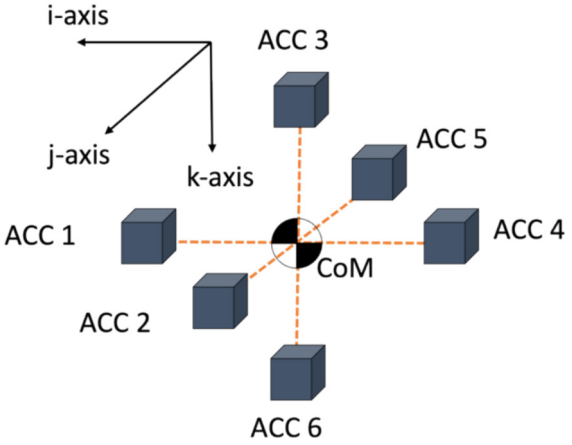

Fig. 12. Accelerometer configuration in the classical GG concept.

$$(\omega_i + s_{\omega,i})^2 \approx \omega_i^2 + 2\omega_i s_{\omega,i}. \tag{53}$$

This relation illustrates the coupling between the angular velocity signal ω_i and the angular velocity noise $\sigma_{\omega,i}$, along the generic axis i.

The errors associated with classical gradiometry are:

$$s^2_{V_{ii}}(f) = \frac{2}{L^2_{\mathrm{GG}}} s^2_{\mathrm{acc,ng}}(f) + 4\Big(\big(\mathrm{RMS}(\omega_j)\big)^2 + \big(\mathrm{RMS}(\omega_k)\big)^2 \Big) s^2_{\omega}(f), \tag{54}$$

where $\mathrm{RMS}(\omega_j)$ and $\mathrm{RMS}(\omega_k)$ are the RMS of the angular velocity signal, which signifies the coupling between signal and noise in the non-linear error propagation. For the pitch rate, we assume $\mathrm{RMS}(\omega_y) \approx 1.1 \times 10^{-3} rad/s$ and for the yaw and roll rate, $\mathrm{RMS}(\omega_x) \approx \mathrm{RMS}(\omega_z) \approx 10^{-4} rad/s$. The underlying assumptions for deriving these RMS values are explained in Appendix 8.1. For the remaining diagonal terms, the corresponding expressions are similar to Eq. (54), considering the RMS of the orthogonal angular velocity components.

The off-diagonal elements of the gravity gradient tensor are given by:

$$\begin{aligned} V_{ij} &= -\frac{a_{2,i} - a_{5,i}}{2L_{\mathrm{GG}}} - \frac{a_{1,j} - a_{4,j}}{2L_{\mathrm{GG}}} + \omega_i \omega_j \\ V_{ik} &= -\frac{a_{1,k} - a_{4,k}}{2L_{\mathrm{GG}}} - \frac{a_{3,i} - a_{6,i}}{2L_{\mathrm{GG}}} + \omega_i \omega_k \\ V_{jk} &= -\frac{a_{3,j} - a_{6,j}}{2L_{\mathrm{GG}}} - \frac{a_{2,k} - a_{5,k}}{2L_{\mathrm{GG}}} + \omega_j \omega_k \end{aligned} \tag{55}$$

Applying error propagation results in:

$$s^2_{V_{ij}}(f) = \frac{1}{L^2_{GG}} s^2_{\mathrm{acc,ng}}(f) + \Big(\big(\mathrm{RMS}(\omega_i)\big)^2 + \big(\mathrm{RMS}(\omega_j)\big)^2 \Big) s^2_{\omega}(f). \tag{56}$$

The expressions for the remaining off-diagonal components are similar, with the RMS of the angular velocity components ω_i, ω_k and ω_j, ω_k relevant to the tensor components ik and jk, respectively.

4.1.2. Attitude reconstruction with classical gradiometers

We analyse the capability of the classical gradiometer to measure angular acceleration and separate gravity gradients from frame rotations. It is fair to assume that the satellite is equipped with star sensors for attitude reconstruction, both on board and in-ground processing. We presume the errors of this instrument are given by Eq. (3).

The GG also functions by design as an accurate angular acceleration sensor, from which the angular velocity can be obtained by numerical integration. The noise ASD of the gradiometer-derived angular accelerations is derived from the accelerometer measurements as follows:

$$\begin{aligned} \dot{\omega}_i &= \frac{a_{2,k} - a_{5,k}}{2L_{\mathrm{GG}}} - \frac{a_{3,j} - a_{6,j}}{2L_{\mathrm{GG}}}, \\ \dot{\omega}_j &= \frac{a_{3,i} - a_{6,i}}{2L_{\mathrm{GG}}} - \frac{a_{1,k} - a_{4,k}}{2L_{\mathrm{GG}}}, \\ \dot{\omega}_k &= \frac{a_{1,j} - a_{4j}}{2L_{\mathrm{GG}}} - \frac{a_{2,i} - a_{5,i}}{2L_{\mathrm{GG}}}. \end{aligned} \tag{57}$$

Since all accelerometer axes have the same performance, we find:

$$s_{\dot{\omega},GG}(f) = \frac{1}{L_{\mathrm{GG}}} s_{\mathrm{acc,ng}}(f), \tag{58}$$

for the noise ASD of the gradiometer-derived angular acceleration measurements, where $s_{\mathrm{acc,ng}}(f)$ is the noise ASD of a linear acceleration measurement of an individual accelerometer. It is worthwhile to note that the angular acceleration measurements derived in this way are more accurate than those of the individual accelerometers, as illustrated in Fig. 13, using MicroSTAR (Section 2.3.1.2) as an example.

The discrepancy between the attitude accuracies in Fig. 13 can be attributed to the small distance (a few centimeters) between the electrodes for the single accelerometer and the larger gradiometer arm (50 cm) that separates the accelerometers.

4.2. Gradiometry with quantum sensors

GG based on quantum sensors relies on generating an initial cloud of atoms that is physically split into two atom clouds, labelled "Cloud 1" and "Cloud 2" in Fig. 14. The advantage is that the relative cloud positions are well-known because the splitting is performed by a laser pulse that gives an accurately known kick to the initial cloud of atoms. Once the two atom clouds are in position, the cold atom interferometric sequence (cf. Section 2.3.2) starts for both atom clouds simultaneously using the same

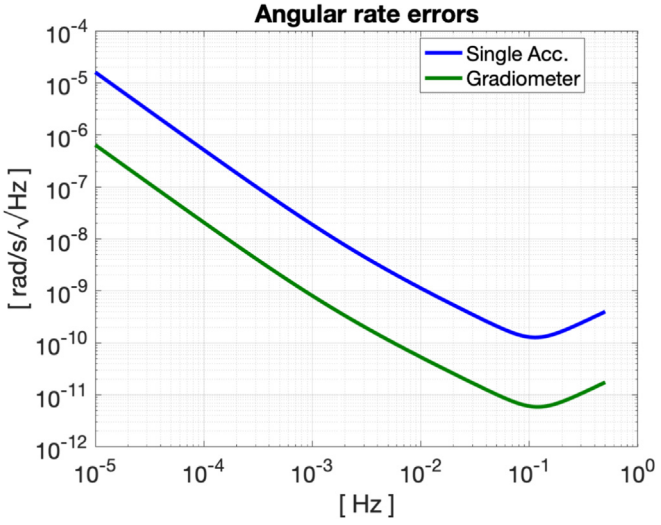

Fig. 13. Noise spectra of the angular velocity derived from the linear acceleration measurements of two accelerometers installed in a gradiometer arm with length $L_{\mathrm{GG}} = 0.5$m (green line) and of the angular acceleration measurements of a single accelerometer (blue line).

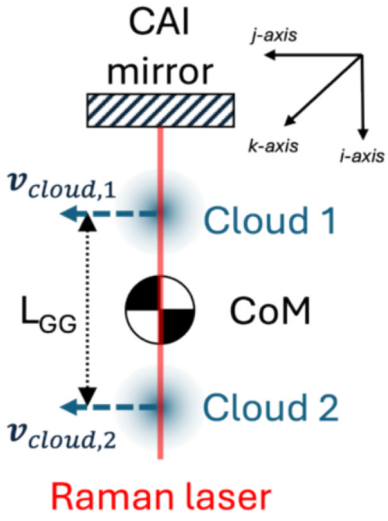

Fig. 14. Quantum GG concept.

Raman laser. In principle, it is the same sequence of laser pulses as for quantum accelerometers. Thus, the quantum gradiometer is also based on sensing the differential acceleration along the laser axis over the precisely known distance between the atom clouds. Consequently, the equations presented in Section 2.3.2 also apply to quantum GG.

By rearranging Eq. (32), we find:

$$\frac{\hbar}{dpT^2}\Phi_{i,l} = \boldsymbol{e}_i \cdot \left(-\boldsymbol{a}_{\mathrm{ng},l} - \left(V - \Omega^2 - \dot{\Omega}\right)\left(\boldsymbol{r}_{\mathrm{cloud},l} - \boldsymbol{r}_{\mathrm{CoM}}\right) + 2\boldsymbol{\omega} \times \boldsymbol{v}_{\mathrm{cloud},l}\right), \tag{59}$$

where $l = 1$ or 2 identifies the atom cloud (cf. Fig. 14). Setting the origin of the reference axis at the CoM, the atom clouds are at positions such that $\boldsymbol{r}_{\mathrm{cloud},1} - \boldsymbol{r}_{\mathrm{cloud},2} \equiv L_{\mathrm{GG}}/2\boldsymbol{e}_i$ at the time the interferometry is done.

Regarding the cloud velocity, we have $\boldsymbol{v}_{\mathrm{cloud},1} = \boldsymbol{v}_{\mathrm{cloud},2}$ and:

$$\begin{aligned}\boldsymbol{v}_{\mathrm{cloud},l} &= \boldsymbol{v}_{\mathrm{cloud,therm},l} + \boldsymbol{v}_{\mathrm{cloud,initial},l} \\ &= \boldsymbol{v}_{\mathrm{cloud,therm},l} + v_{\mathrm{cloud,initial},l}.\boldsymbol{e}_j\end{aligned} \tag{60}$$

In the case of the concurrent mode of operation (Section 2.3.2.1), $\boldsymbol{v}_{\mathrm{cloud,initial},l}$ reflects the transverse velocity imparted by an additional laser perpendicular to the Raman laser axis. In this case, we note that $v_{\mathrm{cloud,initial},1} = v_{\mathrm{cloud,initial},2}$ because both clouds are accelerated with the same recoil laser (not shown in Fig. 14). In the case of the sequential mode, $v_{\mathrm{cloud,initial},1} = v_{\mathrm{cloud,initial},2} = 0$. In both cases, $\boldsymbol{a}_{\mathrm{ng},1} = \boldsymbol{a}_{\mathrm{ng},2}$ because the non-gravitational accelerations affect both clouds equally. As a result, these two terms cancel when computing the differential measurement $\delta\Phi_i \equiv \Phi_{i,1} - \Phi_{i,2}$:

$$\frac{\hbar}{dpT^2}\delta\Phi_i = \boldsymbol{e}_i \cdot \left(-\left(V - \Omega^2 - \dot{\Omega}\right)L_{\mathrm{GG}}\boldsymbol{e}_i + 2\boldsymbol{\omega} \times \boldsymbol{v}_{\mathrm{cloud,therm}}\right), \tag{61}$$

The term on $\boldsymbol{v}_{\mathrm{cloud,therm},l}$ does not cancel because it is related to the thermal velocity of the cloud, which is akin to a random variable.

Recognising that $\dot{\Omega}\boldsymbol{e}_i = \dot{\Omega}\boldsymbol{e}_j = \dot{\Omega}\boldsymbol{e}_k = 0$, cf. Eq. (31), isolating the gravity gradient term, and reducing the vector equation to a scalar quantity results in:

$$\begin{aligned}V_{ii} = &-\frac{1}{L_{\mathrm{GG}}}\frac{\hbar}{dpT^2}\delta\Phi_i - \omega_j^2 - \omega_k^2 \\ &+ \frac{2}{L_{\mathrm{GG}}}\left(\omega_j v_{\mathrm{cloud,therm},k} - \omega_k v_{\mathrm{cloud,therm},j}\right).\end{aligned} \tag{62}$$

The derivation of the equation above and the one for other axes is in Appendix 8.1.2.

4.2.1. Error amplitude of quantum gradiometers

Applying error propagation to Eq. (61), under the assumption that the Raman laser is rotating at the residual angular velocity after compensation by the tilting mirror $\delta\boldsymbol{\omega}$, and considering uncorrelated phase errors, $s^2_{\delta\Phi_i} = s^2_{\Phi_{i,1}} + s^2_{\Phi_{i,2}} = 2s^2_{\Phi}$, results in the errors associated with quantum gradiometry:

$$\begin{aligned}s^2_{V_{ii}} = &\frac{2}{L^2_{\mathrm{GG}}}\frac{T_{\mathrm{cycle}}}{T^4}\frac{s^2_{\Phi_i}}{\beta^2 k^2_{\mathrm{eff}}} + 4\omega_j^2 s^2_{\omega_j} + 4\omega_k^2 s^2_{\omega_k} \\ &+ \frac{16}{L^2_{\mathrm{GG}}}\left(\omega_j^2 s^2_{v_{\mathrm{cloud,therm},k}} + \omega_k^2 s^2_{v_{\mathrm{cloud,therm},j}} + \right. \\ &\left. s^2_{\omega,j} v^2_{\mathrm{cloud,therm},k} + s^2_{\omega,k} v^2_{\mathrm{cloud,therm},j}\right)\end{aligned} \tag{63}$$

Under the conservative assumption of homogeneous noise in all components:

$$\begin{aligned}s^2_V &= \frac{2}{L^2_{\mathrm{GG}}}\frac{T_{\mathrm{cycle}}}{T^4}\frac{s^2_{\Phi_i}}{\beta^2 k^2_{\mathrm{eff}}} + 8\omega^2 s^2_{\omega} \\ &\quad + \frac{32}{L^2_{\mathrm{GG}}}\left(\omega^2 s^2_{v_{\mathrm{cloud,therm}}} + s^2_{\omega} v^2_{\mathrm{cloud,therm}}\right) \\ &\equiv s^2_{V_{\mathrm{CAI}}} + s^2_{\Omega^2} + s^2_{V_{\mathrm{Cor}}} = \frac{2}{L^2_{\mathrm{GG}}}s^2_{\mathrm{CAI,ng}} + s^2_{\Omega^2} + \frac{4}{L^2_{\mathrm{GG}}}s^2_{\mathrm{Cor}},\end{aligned} \tag{64}$$

with expressions for $s_{\mathrm{CAI,ng}}$ and s^2_{Cor} given in Section 3.2.1, and the errors associated with the centrifugal accelerations are $s_{\Omega^2} = \sqrt{8}\omega s_{\omega}$.

4.2.2. Attitude reconstruction with quantum gradiometers

In the case of classical gradiometry (Section 4.1), the 6 capacitive accelerometers that compose the 3D gradiometer make it possible to estimate the rate of change of the attitude (Section 4.1.2). For CAI gradiometry, the case is different since the "accelerometers" are unidimensional. This section examines how single-axis quantum gradiometers can be arranged to provide complete attitude information.

Consider the m-th CAI gradiometer aligned with the i-axis (parallel to $\boldsymbol{e}_i$), shown in Fig. 15.

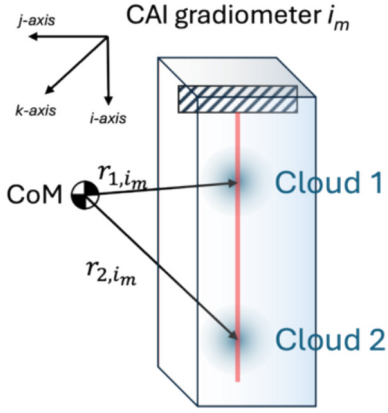

Fig. 15. CAI gradiometer m, aligned with axis i, showing the positions of the atom clouds 1 and 2.

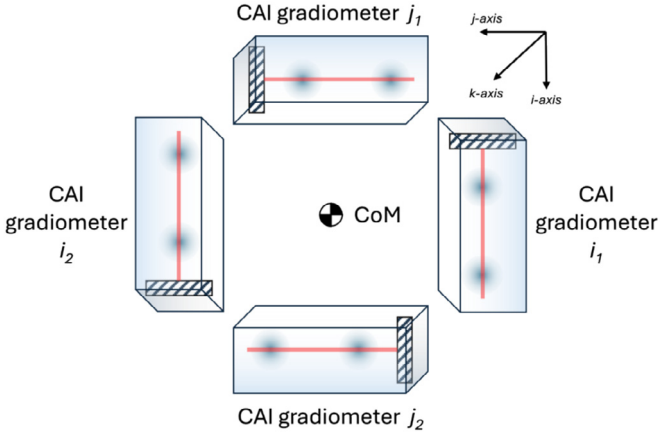

Fig. 16. Arrangement of 4 CAI gradiometers placed symmetrically around the CoM that are able to measure $a_{\mathrm{ng},i}$, $a_{\mathrm{ng},j}$ and $\dot{\omega}_k$.

From Eq. (28), with the reference frame at the CoM, the phase measurement Φ_{l,i_m} of the atom cloud l is:

$$\frac{\Phi_{l,i_m}}{k_{\mathrm{eff}}T^2} = \boldsymbol{e}_i \cdot \left(-\left(\boldsymbol{V} - \Omega^2 - \dot{\Omega}\right)\boldsymbol{r}_{l,i_m} + 2\boldsymbol{\omega} \times \boldsymbol{v}_{\mathrm{cloud}}\right) =$$

$$\boldsymbol{e}_i \cdot \begin{bmatrix} -V_{ii} - \omega_j^2 - \omega_k^2 & -V_{ij} + \omega_i\omega_j - \dot{\omega}_k & -V_{ik} + \omega_i\omega_k + \dot{\omega}_j \\ -V_{ij} + \omega_i\omega_j + \dot{\omega}_k & -V_{jj} - \omega_i^2 - \omega_k^2 & -V_{jk} + \omega_j\omega_k - \dot{\omega}_i \\ -V_{ik} + \omega_i\omega_k - \dot{\omega}_j & -V_{jk} + \omega_j\omega_k + \dot{\omega}_i & -V_{kk} - \omega_i^2 - \omega_j^2 \end{bmatrix} \boldsymbol{r}_{l,i_m} +$$

$$\boldsymbol{e}_i \cdot \begin{bmatrix} \omega_j v_{l,i_m,k} - \omega_k v_{l,i_m,j} \\ \omega_k v_{l,i_m,i} - \omega_i v_{l,i_m,k} \\ \omega_i v_{l,i_m,j} - \omega_j v_{l,i_m,i} \end{bmatrix} + \boldsymbol{e}_i \cdot \boldsymbol{a}_{\mathrm{ng}}. \tag{65}$$

Any linear combination of the two phase measurements Φ_{1,i_m} and Φ_{2,i_m} unavoidably includes off-diagonal terms of $\boldsymbol{V}$, Ω^2 and $\dot{\Omega}$ because $\boldsymbol{r}_{l,i_m}$ is not aligned with $\boldsymbol{e}_i$. Therefore, there are 15 unknowns:

- 6 gravity gradients $\boldsymbol{V}$,
- 3 angular rates $\boldsymbol{\omega}$ (or accelerations $\dot{\Omega}$),
- 3 non-gravitational accelerations $\boldsymbol{a}_{\mathrm{ng}}$ and
- 3 Coriolis accelerations $\boldsymbol{\omega} \times \boldsymbol{v}_{\mathrm{cloud}}$ (or atom cloud velocities $\boldsymbol{v}_{\mathrm{cloud}}$).

In the case of the common and differential linear combinations, 3 degrees of freedom cancel out: the diagonal of the gravity gradient and the non-gravitational accelerations, respectively. In both cases, we are left with 12 unknowns, which require 12 CAI gradiometers to be fully resolved.

One possible arrangement of CAI gradiometers is indicated in Fig. 16 as a "ring" of 4 gradiometer arms arranged symmetrically around the CoM in the same plane, perpendicular to the k-axis, and intersecting the CoM.

The common phase measurement $\sum\Phi_{i1}$ (or $\sum\Phi_{i2}$) and $\sum\Phi_{j1}$ (or $\sum\Phi_{j2}$) of gradiometer i_1 (or i_2) and j_1 (or j_2) provides information on the i-th and j-th component of the non-gravitational accelerations, respectively. The difference between the common phases $\sum\Phi_{i1} - \sum\Phi_{i2}$ or $\sum\Phi_{j1} - \sum\Phi_{j2}$ cancels the Coriolis and non-gravitational accelerations. The sum of the difference of the common phases $\sum\Phi_{i1} - \sum\Phi_{i2} + \sum\Phi_{j1} - \sum\Phi_{j2}$ cancels the gravity gradients and centrifugal accelerations, isolating the $\dot{\omega}_k$ term and, consequently, ω_k by numerical integration. It should be noted that the complete attitude of the satellite could only be determined with the help of an absolute attitude sensor, such as a star tracker, to resolve the attitude bias and bias rate in the case of the proposed CAI gradiometer ring, resulting from the unknown integration constant.

If two orthogonal rings measure the k and j components of the angular acceleration, that would be sufficient to completely retrieve the measurement of the V_{ii}, which would ideally be aligned with the radial direction. The reason is because ω_i does not affect the measurement of V_{ii}. If a third orthogonal ring is added, then the complete diagonal of $\boldsymbol{V}$ is available.

As implied in the analysis in this section, the obvious way to measure attitude independently of gravity effects requires an overly complex instrument. Extrapolating from Trimeche et al. (2019) it would result in an instrument weighing a few tons and requiring several kW of power. This is impractical unless CAI technology can be miniaturized by at least one order of magnitude, while maintaining or improving accuracy.

4.3. Effects of attitude uncertainty of gravity gradiometry

In this section, we analyse the impact of attitude errors similarly to what is done in Section 3.3 for ll-SST. These errors are distinct from the capability of gradiometers to observe attitude rates, analysed in Section 4.1.2 for the classical case, and in Section 4.2.2 for a collection of CAI gradiometers.

The gravity gradients observed in the SRF $\boldsymbol{V}^{(}\mathrm{SRF})$ are related to the gravity gradients in the ECEF reference frame $\boldsymbol{V}^{(}\mathrm{ECEF})$ by:

$$\boldsymbol{V}^{(}\mathrm{ECEF}) = \boldsymbol{R}^{(}\mathrm{ECEF[LFTARW]SRF})\boldsymbol{V}^{(}\mathrm{SRF})\boldsymbol{R}^{(}\mathrm{ECEF[LFTARW]SRF})^{T}, \tag{66}$$

where $\boldsymbol{R}^{(}\mathrm{ECEF[LFTARW]SRF})$ is the rotation that transforms from the satellite to the ECEF reference frame. The attitude measurements generally relate the ECI frame to the SRF frame, so it makes more sense to split the rotation in these frames:

$$\boldsymbol{V}^{(}\mathrm{ECEF}) = \boldsymbol{R}^{(}\mathrm{ECEF[LFTARW]ECI})\boldsymbol{R}^{(}\mathrm{ECI[LFTARW]SRF})\boldsymbol{V}^{(}\mathrm{SRF})\boldsymbol{R}^{(}\mathrm{ECI[LFTARW]SRF})^{T}\boldsymbol{R}^{(}\mathrm{ECEF[LFTARW]ECI})^{T}. \tag{67}$$

Assuming the ECI to ECEF frame is known perfectly, we can focus on the gravity gradients in the ECI frame:

$$\boldsymbol{V}^{(}\mathrm{ECI}) = \boldsymbol{R}^{(}\mathrm{ECI[LFTARW]SRF})\boldsymbol{V}^{(}\mathrm{SRF})\boldsymbol{R}^{(}\mathrm{ECI[LFTARW]SRF})^{T}. \tag{68}$$

As for ll-SST, Section 3.3, we model the transformation $\boldsymbol{R}^{(}\mathrm{ECI[LFTARW]SRF})$ as the product of the error-free rotation $\boldsymbol{R}^{(}\mathrm{ECI[LFTARW]SRF, true})$ and a small-angle rotation matrix $\Theta^{(}\mathrm{ECI[LFTARW]SRF})$:

$$\boldsymbol{R}^{(}\mathrm{ECI[LFTARW]SRF}) = \boldsymbol{R}^{(}\mathrm{ECI[LFTARW]SRF, true})\Theta^{(}\mathrm{ECI[LFTARW]SRF}), \tag{69}$$

and Eq. (66) becomes:

$$\boldsymbol{V}^{(}\mathrm{ECI}) = \boldsymbol{R}^{(}\mathrm{ECI[LFTARW]SRF, true})\Theta^{(}\mathrm{ECI[LFTARW]SRF})\boldsymbol{V}^{(}\mathrm{SRF})\Theta^{(}\mathrm{ECI[LFTARW]SRF})^{\mathrm{T}}\boldsymbol{R}^{(}\mathrm{ECI[LFTARW]SRF, true})^{\mathrm{T}}. \tag{70}$$

If we restrict our analysis to the terms that contain errors, we can safely ignore the error-free transformation $\boldsymbol{R}^{(}\mathrm{ECI[LFTARW]SRF, true})$:

$$\boldsymbol{V}^{(}\mathrm{ECI}) = \Theta^{(}\mathrm{ECI[LFTARW]SRF})\boldsymbol{V}^{(}\mathrm{SRF})\Theta^{(}\mathrm{ECI[LFTARW]SRF})^{\mathrm{T}}, \tag{71}$$

We split $\Theta^{(}\mathrm{ECI[LFTARW]SRF}) = \boldsymbol{E} + \boldsymbol{I}$ as before and drop the reference frame superscript:

$$\boldsymbol{V}^{(}\mathrm{ECI}) = (\boldsymbol{I} + \boldsymbol{E})\,\boldsymbol{V}^{(}\mathrm{SRF})(\boldsymbol{I} + \boldsymbol{E})^{\mathrm{T}} \tag{72}$$

As usual, the error propagation of Eq. (72) requires the tensor $\boldsymbol{V}^{(}\mathrm{ECI})$ to be collapsed into vector, $\boldsymbol{v}^{(}\mathrm{ECI})$, producing the error 9×9 covariance matrix $\boldsymbol{C}_{\boldsymbol{V}}$:

$$\boldsymbol{C}_{\boldsymbol{V}} = \nabla\boldsymbol{v}^{(}\mathrm{ECI})[s_\theta]\nabla\boldsymbol{v}^{(}\mathrm{ECI})^{\mathrm{T}} \tag{73}$$

In evaluating Eq. (73), we assume that $\boldsymbol{V}$ is error-free, the small angles are negligible $\theta_{\mathrm{roll,s}} = \theta_{\mathrm{pitch,s}} = \theta_{\mathrm{yaw,s}} \approx 0$, and we ignore the cross-correlations such that $[s_{\boldsymbol{V},\theta}] = \mathrm{diag}(\boldsymbol{C}_{\boldsymbol{V}})$, resulting in

$$\begin{bmatrix} s^2_{V_{xx},\theta} \\ s^2_{V_{yy},\theta} \\ s^2_{V_{zz},\theta} \\ s^2_{V_{xy},\theta} \\ s^2_{V_{xz},\theta} \\ s^2_{V_{yz},\theta} \end{bmatrix} = \begin{bmatrix} 0 & 4V^2_{xz} & 4V^2_{xy} \\ 4V^2_{yz} & 0 & 4V^2_{xy} \\ 4V^2_{yz} & 4V^2_{xz} & 0 \\ V^2_{xz} & V^2_{yz} & (V_{xx} - V_{yy})^2 \\ V^2_{xy} & (V_{xx} - V_{zz})^2 & V^2_{yz} \\ (V_{yy} - V_{zz})^2 & V^2_{xy} & V^2_{xz} \end{bmatrix} \begin{bmatrix} s^2_{\theta_{\mathrm{roll}}} \\ s^2_{\theta_{\mathrm{pitch}}} \\ s^2_{\theta_{\mathrm{yaw}}} \end{bmatrix}. \tag{74}$$

Considering the amplitude of the gravity gradient signal presented in Section 8.4 and setting the errors $\boldsymbol{s}_\theta$ equal to 1, the scaling of the attitude errors into gravity gradient errors is:

$$[s_{\boldsymbol{V},\theta}] = \begin{bmatrix} 0.2 & 5 & 3600 \\ 9.7 & 3603 & \\ 9.7 & & \end{bmatrix} \times 10^{-3} E$$

5. Results and discussion

We present our results by quantifying the amplitude of frame accelerations, specifically those related to the effects of Coriolis accelerations and centrifugal accelerations, in Section 5.1. We quantify the errors for ll-SST in Section 5.2 for both electrostatic (Section 5.2.1) and quantum (Section 5.2.2) accelerometers. Finally, we quantify the errors for quantum gradiometry in Section 5.3 for the gradiometer operating in sequential mode.

5.1. Importance of the frame accelerations

In this section, we quantify the amplitude of the Coriolis and centrifugal accelerations. CAI accelerometry is only affected by the former (Section 3.2.1), while gradiometry is affected by both (Section 4.2.1).

Recall that the variance of the Coriolis term $\sigma^2_{\mathrm{Cor},i}$ in a CAI accelerometer aligned with the i-axis, cf. Eqs. (35) and (36), are:

$$s^2_{\mathrm{Cor},i} = 4\omega^2_j s^2_{v,\mathrm{cloud},k} + 4\omega^2_k s^2_{v,\mathrm{cloud},j} + 4s^2_{\omega,j} v^2_{\mathrm{cloud},k} + 4s^2_{\omega,k} v^2_{\mathrm{cloud},j} \tag{75}$$

which is valid for both along-track and cross-track ll-SST.

Suppose the CAI mission concept under analysis assumes attitude compensation with a tilting mirror. In that case, the angular velocity ω_i in Eq. (75) is not the satellite angular velocity but the residual angular velocity after attitude compensation. Therefore, the symbol $\delta\omega$ aims to indicate when a result is relevant to this case. We develop all equations using the original symbol for angular velocity ω, ensuring they apply to the general case.

The mean angular velocity of a nadir-pointing satellite in LEO is the pitch rate of about $\omega_y = 1.1 \times 10^{-3}\mathrm{rad/s}$, with the y-axis aligned with the cross-track direction. The yaw and roll rate are typically at least one order of magnitude smaller, i.e., about $\omega_x = \omega_z = 1 \times 10^{-4}\mathrm{rad/s}$ (Allasio et al., 2010), with the x-axis aligned with the along-track direction and the z-axis right-hand orthogonal (which is parallel to the radial direction in a circular orbit).

The compensation of the angular velocity requires that either the satellite attitude or the tilting mirrors be controlled, taking input from a sensor that provides angular velocity measurements. One of the best-performing angular velocity sensors is the Astrix 200 laser gyroscope, which has an accuracy of $s_\omega = 5 \times 10^{-8}\mathrm{rad/s}$. We believe that it will

not be possible to control the attitude of the tilting mirrors in real-time with the same level of accuracy as measured by the gyroscope. For this reason, we assume a conservative accuracy degradation given by the factor f_ω:

$$\delta\omega = f_\omega s_\omega, \tag{76}$$

taken to be one order of magnitude, $f_\omega = 10$, worse than the measurement system, i.e., $\delta\omega = 5 \times 10^{-7}$rad/s for the case of the mirror compensating the satellite rotation driven by the Astrix 200 gyroscope. This is a conservative assumption, as experiments on the China Space Station have shown comparable error levels between the attitude derived from the piezoelectric mirror and an external gyroscope (Li et al., 2025). In Section 0, the satellite rotation is compensated in this way, and we assume $\boldsymbol{\omega} = \delta\boldsymbol{\omega}$.

We only consider attitude compensation for cases involving quantum accelerometry or gradiometry, and not for electrostatic accelerometers or classical gradiometers, for example, by physically rotating the instrument within the satellite body.

We here consider a number of scenarios. The *full attitude compensation* scenario assumes $\delta\omega = 5 \times 10^{-7}$rad/s in all directions. In the *no tilting mirror* scenario, we assume $\omega = 1 \times 10^{-4}$rad/s for yaw and roll and $\omega = 1.1 \times 10^{-3}$rad/s for pitch, as mentioned above. We also consider the intermediate case of *minimum pitch-rate compensation*, where the pitch is compensated to the level of $\delta\omega = 1 \times 10^{-4}$rad/s.

For the atom cloud velocity, we assume that either one component is $v_{\text{cloud,j}} = 2.5$cm/s and the other components are zero in the case of the concurrent operational mode, or all atom cloud velocity components are zero in the case of the sequential mode of operation (cf. Section 2.3.2.1). For the uncertainty in the atom cloud velocity $s_{v_{\text{cloud}}}$, we assume DKC with $v_{\text{atom,therm}} = 10^{-6}$m/s and $s_{v_{\text{cloud,initial}}} = 10^{-7}$m/s; from Eqs. (38) and (39), we determine that $s_{v_{\text{cloud,therm}}} = 2.3 \times 10^{-10}$m/s for $N = 10^6$.

Under these assumptions, we can quantify the effect of the Coriolis term for both concurrent and sequential operational modes, combined with different levels of attitude compensation, as summarized in Table 1.

In the concurrent case, the Coriolis effect is dominated by the large cloud velocity and is insensitive to attitude compensation. Therefore, the only possibility for a CAI accelerometer to outperform the MicroSTAR accelerometer, which has a precision of 2×10^{-12}m/s^2 (cf. Section 2.3.1.2), is to consider full attitude compensation and zero atom cloud velocity provided by the sequential mode of operation. This choice limits the measurement cycle to be equal to the interrogation time, as explained in Section 2.3.2.1.

To make the concurrent mode of operation competitive, one would have to reduce the initial cloud velocity to at least 10^{-5}m/s for the Coriolis effects to reach the level of 10^{-12}m/s^2. This extremely slow velocity would increase the sampling time prohibitively, and it becomes preferable to cycle through interferometry and atom production sequentially. The only other option is to decrease the attitude uncertainty by three orders of magnitude, which is very technically challenging for classical attitude sensors; for example, ground equipment is only at best two orders of magnitude better (Stedman et al., 2003).

For CAI gradiometry, the effect of the Coriolis accelerations in Eq. (64) is:

$$s_{V_{\text{Cor}}} = \frac{2}{L_{GG}} s_{\text{Cor}}, \tag{77}$$

which effectively means that noise in the gravity gradients is a factor of 4 worse compared to CAI accelerometers, assuming $L_{GG} = 0.5$m. In addition to that, the problem is exacerbated by the small, time-variable gravity gradient signal shown in Fig. 9. A gradiometer operating in sequential mode with full attitude compensation would have $s_{V_{\text{Cor}}} = 0.8\text{mE} = 8.0 \times 10^{-13}\text{s}^{-2}$, which is insufficient to sense the time-variable gravity field. We note that this discussion is exclusively based on the effect of the Coriolis force, with no regard to the CAI interferometric sensitivity discussed in Section 2.3.2.

The amplitude of the effect of the centrifugal accelerations is $s_{\Omega^2} = \sqrt{8}\delta\omega\sigma_\omega$, which follows from Eq. (64). Continuing with the assumption that the angular rate has noise of $s_\omega = 5 \times 10^{-8}$rad/s and that ω is related to the tilting mirror compensation $\delta\omega = 5 \times 10^{-7}$rad/s, we expect $s_{\Omega^2} = 0.071$mE. Consequently, unlike the Coriolis forces, the centrifugal accelerations do not limit the CAI gradiometer's sensitivity to temporal variations of the gravity field.

Table 1
Standard deviation of the Coriolis term $\sigma_{\text{Cor},i}$, assuming $\sigma_{\omega,j} = \sigma_{\omega,j} = 5 \times 10^{-8}$ rad/s, $v_{\text{atom,therm}} = 10^{-6}$m/s and $\sigma_{v_{\text{cloud,initial}}} = 10^{-7}$m/s for several combinations of angular velocity compensation scenarios and operational modes (affecting the cloud velocity), for the case of along-track ll-SST and the *i*-axis aligned with the along-track direction.

Attitude compensationscenario	Residual angular velocity [rad/s]	Concurrent mode [m/s^2] $v_{\text{cloud,k}} = \sigma_{v_{\text{cloud,therm}}} = 0.23\text{nm/s} v_{\text{cloud,j}} = 2.5\text{cm/s}$	Sequential mode [m/s^2] $v_{\text{cloud,k}} = v_{\text{cloud,j}} = \sigma_{v_{\text{cloud,therm}}} = 0.23\text{nm/s}$
No tilting mirror	$\omega_j = 1.1 \times 10^{-3} \omega_k = 10^{-4}$	2.5×10^{-9}	2.2×10^{-10}
Minimum pitch-rate compensation	$\delta\omega_j = \omega_k = 10^{-4}$	2.5×10^{-9}	2.8×10^{-11}
Full attitude compensation	$\delta\omega_j = \delta\omega_k = 5 \times 10^{-7}$	2.5×10^{-9}	2.0×10^{-13}

5.2. ll-SST

In this analysis, we include the effects of attitude uncertainty presented in Section 3.3, for which the magnitude of non-gravitational accelerations is important. We consider the 2 scenarios motivated in Section 8.3: the RMS of the non-gravitational accelerations experienced at 230 km and the residual non-gravitational accelerations with a 3D DFC system at the same altitude. We note that we have omitted the case of the 1D DFC system, similar to GOCE, because it is identical to the *no DFC* scenario since the y and z-axis non-gravitational accelerations are relevant to the case where the ISR axis is (roughly) aligned with the x-direction. These are the same for the two considered DFC scenarios, as noted in Eq. (50).

5.2.1. Electrostatic accelerometry

We start our analysis of the ll-SST future gravimetric missions with the case of electrostatic accelerometry. The three DFC scenarios differently amplify the attitude errors s_ω, for which we assume 3 scenarios: DWS of LISA (Section 2.1.3.1), DWS of GRACE-FO (Section 2.1.3.2), and no DWS. In all scenarios, the measurements of the sensors above are optimally combined with the attitude measurements from the star tracker (Section 2.1.1), Astrix 200 laser gyroscope (Section 2.1.2), and accelerometer (Section 2.1.4). The results are shown in Fig. 17, along with the predicted performance of the ISR instrument in 2040 (Section 2.2.4), and the errors of the MicroSTAR accelerometer (Section 2.3.1.2).

The main message of Fig. 17 is that the components of the time-variable gravity field model (black dotted line) are fully observed up to 30 mHz, or roughly SH degree 170, assuming sufficiently dense ground track coverage over a reasonably short period. At this frequency, the signal represented by the black dotted line crosses both the errors in the accelerometer and the ISR instrument. The high accuracy of the ISR instrument is not fully utilized below this frequency due to insufficient accelerometer performance, as indicated by the yellow line being above the pink line.

The attitude errors are insignificant for the majority of the scenarios. We predict that the need for DFC is only necessary if DWS is not available (red dotted line), which is unlikely, as it has already been demonstrated for GRACE-FO.

5.2.2. Quantum accelerometry

To fully utilize the high accuracy of the ISR instrument predicted for 2040 (Section 2.2.4), we propose the CAI accelerometer listed in Table 2.

We selected the parameters in Table 2 so that the noise amplitude of the CAI accelerometer is below the noise floor of the ISR 2040 instrument, as shown in Fig. 18 We do not intend to claim that the illustrated parameters and performances are realistically achievable within a fixed timeframe; rather, we aim to offer a balanced conceptual view

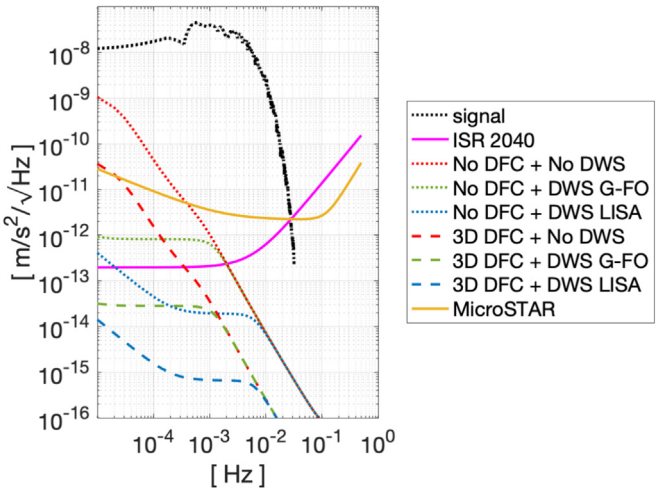

Fig. 17. Effect of the attitude errors for no (red, blue and green dotted lines) and 3D (red, blue and green dashed lines) DFC with three different combinations of attitude instruments indicated in the legend plus the attitude derived from the μASC star tracker and accelerometer, compared to the errors of the accelerometer (solid yellow line), ISR errors predicted for 2040 (solid pink line), and the estimated time-variable signal magnitude (dotted black line).

of a feasible configuration. Future advances may shift the relative cost and feasibility of individual parameters, leading to alternative, more efficient configurations. For example, we observe that the two most critical parameters are the degree of entanglement, due to the very low maturity of the required engineering solutions, and the number of atoms, which has reached the highest level to date of only 10^6, over a few seconds (Rudolph et al., 2015).

For this analysis, we maintained the DFC and attitude scenarios of Section 5.2.1, with the exception that the accelerometer-derived attitude is not available. For the Coriolis effects, we considered only one scenario: DWS of GRACE-FO (Section 2.1.3.2), star tracker (Section 2.1.1), and Astrix 200 laser gyroscope (Section 2.1.2); the case with LISA DWS yields a reduced amplitude of the Coriolis effects (not shown) but with no change to the interpretation of the results.

In the case of the CAI accelerometer operating in concurrent mode, the noise amplitude is dominated by the Coriolis effect (purple dashed line) due to the non-zero cloud velocity, as explained in Section 5.1, with a noise floor two orders of magnitude above the CAI sensitivity (solid purple line). With such an instrument, not even GRACE's KBR would operate at full capacity, cf. Fig. 4. In contrast, this instrument operating in sequential mode has a sensitivity (solid yellow line) a factor of 3 worse than in concurrent mode, as a result of the reduced sampling rate, Eq. (21), but a much-reduced effect of the Coriolis accelerations (dashed yellow line), with a noise floor two orders of magnitude below (4 orders of magnitude if compared to the Coriolis effects of the concurrent mode of operation) and reaching the amplitude of the CAI sensitivity at 3 mHz.

Table 2
CAI parameters.

Parameter	Equation	Symbol	Value
Laser wavelength	(16)	λ	780nm
Number of atoms	(17)	N	10^7
Interferometer contrast	(17)	C	0.8
Degree of entanglement	(17)	α	0.25
Momentum space separation	(18)	β	2
Interrogation time	(20)	T	5s
Measurement cycle period	(21)	T_{cycle}	1s
Atom thermal velocity	(37)(38)	$v_{\text{atom, therm}}$	10^{-6}m/s
Initial cloud velocity error	N/A	$s_{v_{\text{cloud,initial}}}$	10^{-7}m/s
Cloud velocity	(39)	v_{cloud}	0or 2.5cm/s
Attitude accuracy degradation factor	(76)	f_ω	10

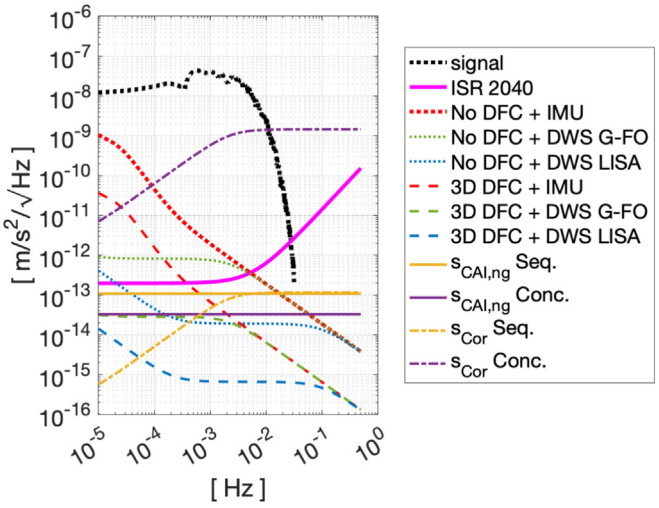

Fig. 18. Comparison of the effect of attitude errors (dotted and dashed red, blue and green lines, Section 3.3) with the ISR errors predicted for 2040 (Section 2.2.4, solid pink line, identical to Fig. 17) and the estimated time-variable signal magnitude (dotted black line, similar to Fig. 17), with the errors of the CAI accelerometer operating under the sequential mode (yellow lines) and concurrent mode (purple lines, cf. Section 2.3.2.1), distinguished between the CAI sensitivity (solid purple and yellow lines, Section 2.3.2) and Coriolis effects (dot-dashed purple and yellow lines, Section 3.2.1).

The temporal signal is resolved up to 30 mHz, or SH degree 170, which is the same as electrostatic case (Section 5.2.1). Unlike the electrostatic case, the quantum accelerometer is more accurate than the LTI at all frequencies, and the time-variable signal is measured with an SNR of 10^4 at 10 mHz (SH degree 57). This provides a strong indication that this gravimetric mission would be much less susceptible to errors in the low-degree coefficients that plague the GRACE and GRACE-FO gravity field models.

As for attitude and DFC options, the situation is much more demanding than electrostatic accelerometry. For quantum accelerometry, there is a need for LISA-level DWS if DFC is unavailable (dotted blue line). If 3D DFC is available, GRACE-FO's DWS is sufficient (dashed green line). This result illustrates the strict attitude requirements that the increased sensitivity of quantum accelerometers demands on the accuracy of the attitude data.

5.3. Gradiometry

In Section 5.1, we quantify the effect of the Coriolis accelerations $s_{V_{\text{Cor}}}$ under the assumption of white noise for the attitude measured by the Astrix 200 laser gyroscope. In reality, the spectra of the errors of this instrument do not exhibit a constant amplitude with frequency, as shown in Section 2.1.2. Additionally, the combination with other attitude instruments was not quantified. We do not consider classical gradiometry because electrostatic accelerometers lack the necessary accuracy to observe the time-variable gravity signal, as shown in Fig. 9.

We compare the error spectra of the Coriolis and centrifugal terms with the CAI sensitivity in Table 2, thus making the ll-SST (discussed in Section 5.2.2) and gradiometry cases directly comparable. We only consider the sequential mode of operation (cf. Section 2.3.2.1) because of the destructive effect of the Coriolis accelerations already demonstrated for the ll-SST case. To examine the impact of attitude uncertainty presented in Sections 3.3 and 4.3 for ll-SST and GG, respectively, we consider the gravity gradient signal amplitudes discussed in Section 8.4. Unlike the ll-SST case, drag compensation is not relevant to the errors we analyse in this section because it only affects the non-gravitational signal amplitude. We consider that attitude is measured with the star tracker (Section 2.1.1), Astrix 200 laser gyroscope (Section 2.1.2), and accelerometer (Section 2.1.4). We include the attitude derived from the accelerometer, as demonstrating an early CAI gradiometer in space would benefit from validation with proven instruments, such as an electrostatic accelerometer. Additionally, this instrument reduces the amplitude of the attitude errors above 0.7 mHz, Fig. 1, which is critical for collecting the small time-variable gravity field disturbances. The results of this analysis are presented in Fig. 19.

Although the gradiometer CAI sensitivity (red line) is barely enough to resolve the time-variable gravity signal

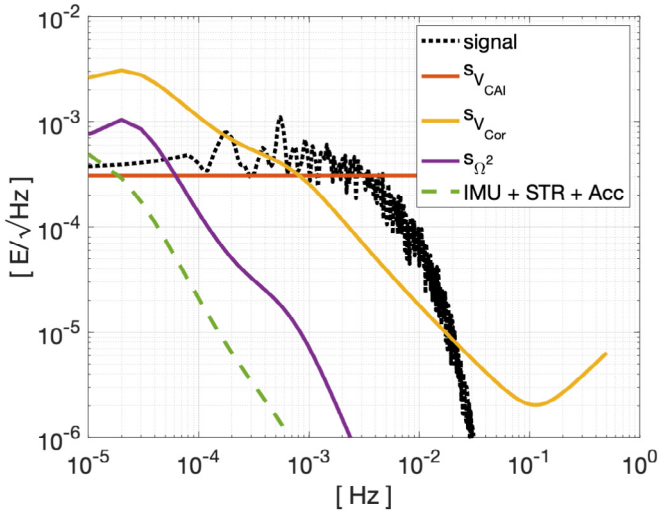

Fig. 19. Comparison of the effect of attitude errors (dashed green line, Section 4.3) with the time-variable gravity gradient signal (dotted black line, same as Fig. 9) gradiometer CAI sensitivity (red line, Section 4.2), the Coriolis effect (yellow line, Section 4.2) and the effects of centrifugal accelerations (purple line, Section 4.2), as measured by the IMU (Section 2.1.2), star tracker (Section 2.1.1) and attitude derived from the electrostatic accelerometer (Section 2.1.4).

(black dotted line) up to 3 mHz, corresponding roughly to SH degree 17, the Coriolis effects (yellow line) make it impossible to observe this signal below 0.4 mHz or SH degree 2. The impact of attitude uncertainty (purple line) is at least an order of magnitude below the Coriolis effects and only surpasses the magnitude of the gradiometer CAI sensitivity below 0.02 mHz. Notably, the Coriolis errors (and those associated with centrifugal and attitude errors) are solely a function of the attitude sensors and remain unchanged even if more accurate CAI gradiometers are considered. Therefore, CAI gradiometry requires a novel attitude determination system, which is currently unavailable.

In contrast to the ll-SST case using quantum accelerometers (Section 5.2.2), where the complete signal spectrum is resolved with a high SNR, the quantum gradiometer with the same CAI parameters is barely able to determine the time variable signal, with an SNR mostly between 1 and 2, peaking at 3 and dipping at 0.5 at some frequencies.

This example underscores the importance of the high accuracy of all instruments in the success of CAI gradiometry. Although quantum technology may enable extremely high CAI sensitivities, a proportional improvement in the attitude sensors is necessary.

6. Summary and discussions

In this study, we model the sensitivity of a CAI accelerometer as a function of interferometry contrast, degree of entanglement, number of atoms, momentum space separation and interrogation period (Section 2.3.2). We assume the CAI gradiometer is composed of two CAI accelerometers in the form of two cloud pairs in the same interferometric chamber. In this way, we model quantum gradiometry in a similar way to classical gradiometry, i.e., that the latter is composed of two electrostatic accelerometers. One important difference is that a CAI accelerometer is inherently a one-dimensional instrument, unlike the electrostatic accelerometer. However, this is irrelevant for the diagonal components of the gravity gradient tensor. We intend to make a straightforward application of the currently proposed architectures for CAI instruments, without suggesting or discussing advanced options, such as vectors CAI accelerometers (Barrett et al., 2019), CAI instruments that are also able to observe angular accelerations (Li et al., 2025), or bridging options like classical/quantum hybrid accelerometers (HosseiniArani et al., 2025).

We present electrostatic and quantum accelerometers for ll-SST and gradiometer satellite mission concepts, modelling the measurements and their errors analytically (Section 3). The attitude determination received special attention, particularly in modeling the propagation of associated errors to the observations collected by the accelerometers and gradiometers. For electrostatic accelerometers, the instrument provides attitude information directly since there are multiple electrodes in each facet of the proof mass cavity (Section 2.1.4). On the other hand, so far, no attitude data can be measured by a quantum accelerometer. For classical gradiometry, attitude is estimated with one order of magnitude better accuracy than the electrostatic accelerometer (Section 4.1.2). For quantum gradiometry, we demonstrate that 12 uniaxial CAI gradiometers are required to resolve the satellite's attitude (Section 4.2.2). This results in an overly complex instrument that is feasible only if CAI technology can be miniaturised.

To mitigate the impact of inaccurately known angular rates on Coriolis accelerations in quantum instruments, as defined analytically in Section 3.2.1 for CAI accelerometers and in Section 4.2.1 for CAI gradiometers, we distinguish between concurrent and sequential modes of operation the former enables a higher sampling rate and accuracy. The latter minimises atom cloud velocity and, consequently, Coriolis accelerations (Section 2.3.2.1). In Section 5.1, we demonstrate that CAI accelerometry operating in the concurrent mode results in prohibitively high effects due to Coriolis accelerations, limiting the sensitivity of any CAI accelerometer to $s_{\mathrm{Cor}} = 2.5 \times 10^{-9}\mathrm{m/s^2}$, for which we assume an initial cloud velocity error of $s_{v_{\mathrm{cloud,initial}}} = 10^{-7}\mathrm{m/s}$, a thermal cloud velocity of $v_{\mathrm{atom,therm}} = 10^{-6}\mathrm{m/s}$ and a transverse cloud velocity of $v_{\mathrm{cloud}} = 2.5\mathrm{cm/s}$. For the sequential mode of operation, the cloud velocity is solely associated with thermal motion, and the Coriolis effects are limited to $s_{\mathrm{Cor}} = 2.0 \times 10^{-13}\mathrm{m/s^2}$, which includes the impact of the necessary lower sampling rate compared to the concurrent operational mode. Either case requires full attitude com-

pensation with tilting mirrors, which reduces the satellite's attitude rates down to 5×10^{-7}rad/s, assumed to be one order of magnitude worse than what the high-performance Astrix 200 laser gyroscope can measure (Section 2.1.2). Although such a CAI instrument is well-suited as an accelerometer for ll-SST, it is unable to measure temporal gravity changes as a gradiometer, since the sensitivity would be limited to $s_{V_{\mathrm{Cor}}} = 0.8$mE for a distance between cloud-pairs (i.e., the gradiometer arm length) of $L_{GG} = 0.5$m.

We considered the errors related to the rotation of the measurements in the body (for gradiometry) or local (for ll-SST) frames to the Earth corotating frame (Section 4.3), which are important given the high accuracy of the measurements and the potential for a large acceleration or gravity gradient signal at LEO altitudes. These errors relate the signal amplitude of non-gravitational accelerations (for accelerometers) or gravity gradient amplitudes (for gradiometry) to the attitude accuracy. They become important when the attitude measurements have limited accuracy, as is the case with classical attitude sensors. At the same time, the signal can be measured with increased accuracy, for example, with predicted quantum sensors. An example is the case of ll-SST equipped with a CAI accelerometer, Section 5.2.2, where the need for a 3D DFC system is required in the case the attitude derived with the DWS is retrieved with accuracy comparable to what GRACE-FO is capable of; if this can be done with an accuracy predicted for LISA, then no DFC is necessary.

In Section 5.2.2, we consider a CAI accelerometer with a noise level of $s_{\mathrm{CAI,ng}} = 3.2 \times 10^{-14}\mathrm{m/s^2}$ in the concurrent mode and $s_{\mathrm{CAI,ng}} = 1.1 \times 10^{-13}\mathrm{m/s^2}$ in the sequential mode, with the CAI parameters in Table 2. Notably, the degree of entanglement is $\alpha = 0.25$, the number of atoms is $N = 10^7$, and the momentum space separation $\beta = 2$ is associated with a second kick. This example scenario illustrates a possible path for the development of CAI instruments with increasing accuracy and their capabilities for gradiometry. In case of the instrument operating in sequential mode in an ll-SST formation, its sensitivity is not significantly limited by the effects of the Coriolis accelerations, since they have an amplitude of $s_{\mathrm{Cor}} = 1.2 \times 10^{-13}\mathrm{m/s^2}$. As a result, the LTI predicted for 2040 is not hampered in any way down to the sub-orbital frequencies. In contrast, in the case of ll-SST with an electrostatic accelerometer (Section 5.2.1), the MicroSTAR electrostatic accelerometer noise spectrum dominates over the LTI in all frequencies below 30 mHz.

In Section 5.3, we apply the CAI parameters derived for the case of ll-SST to quantum gradiometry, using the CAI operating in sequential mode. We demonstrate that, unlike the case for ll-SST, this instrument is barely sensitive enough to resolve temporal changes in Earth's gravity. The maximum SH degree it is sensitive to is 17, and the Coriolis accelerations make it impossible to measure spatial features with a length associated with SH degree 2 or longer. This example illustrates the significantly reduced gravity gradient signal amplitude compared to gravitational accelerations to which ll-SST is sensitive.

We recognise that there are important technological challenges associated with the solutions considered in this study. We have generally neglected such details because our analysis is restricted to the conceptual level. The obvious consequence is the high cost for the necessary technical and engineering developments, most notably those associated with i) the highly accurate rotation compensation provided by the tilting mirrors and ii) the cooling of the atom cloud during the BEC preparation that is required to reduce the thermal velocity of the atoms as assumed in this study. We also note that we did not model the loss of interferometric contrast associated with the scenarios without rotation compensation, as this parameter is specific to the instrument's design.

Nevertheless, we have demonstrated that the effects of inaccurately measured attitude in the Coriolis accelerations are of paramount importance to the success of the CAI satellite gravimetry, even in the quiet environment of space. We emphasise that this is a problem that cannot be solved with novel attitude control strategies (Zinage et al., 2024) or eventual advanced ground processing techniques. There is a limitation in observing the spacecraft's attitude with unprecedented accuracy, which is necessary to ensure that the high-quality data collected by the CAI instrument is fully exploited. Until this is done, it is significantly less technically challenging to implement gravimetric CAI technology in the context of the ll-SST measurement concepts. We also demonstrate that it is much easier to take advantage of the CAI accelerometer operating in sequential mode to circumvent the limitations of attitude data quality. We further contextualize that this conclusion is a result of the study's limitations; therefore, any significant improvement in the attitude data quality, especially if gathered by the CAI instrument itself, would effectively unleash the full potential of CAI gradiometry.

Declaration of competing interest

The authors declare that they have no known competing financial interests or personal relationships that could have appeared to influence the work reported in this paper.

Acknowledgements

The work presented in this paper was conducted within the framework of the European Space Agency (ESA) study, entitled *Quantum Space Gravimetry for monitoring Earth's Mass Transport Processes* (QSG4EMT). The QSG4EMT study has the objective to analyse QSG mission architectures that can optimally recover the time variable gravity field of the Earth, which relates to mass transport processes of interest for operational applications, as well as for Earth Sciences, and propose candidate QSG mission concepts with mission requirements that advance the science and satisfy the needs of the user community to a

greater extent than the state-of-the-art and planned missions.

We thank Vitali Müller, from the Albert-Einstein-Institut in Hannover, for the insightful predictions of the LTI performance in the near future.

Appendix. *Derivations*

CAI accelerometer observation equation

Assume that the axis of the Raman laser is aligned with the i-axis:

$$\frac{\boldsymbol{k}_{\text{eff}}}{k_{\text{eff}}} = \boldsymbol{e}_i.$$

Starting from Eq. (26):

$$\Phi = \boldsymbol{k}_{\text{eff}} \cdot (\boldsymbol{a}_{\text{cloud}} - \boldsymbol{a}_{\text{mirror}}) T^2$$

The non-gravitation accelerations are given by $\boldsymbol{a}_{\text{ng}} = \boldsymbol{a}_{\text{mirror}}$, or:

$$\Phi = \boldsymbol{k}_{\text{eff}} \cdot \left(\boldsymbol{a}_{\text{cloud}} - \boldsymbol{a}_{\text{ng}}\right) T^2$$

$$\frac{\Phi}{k_{\text{eff}}} = \frac{\boldsymbol{k}_{\text{eff}}}{k_{\text{eff}}} \cdot \left(\boldsymbol{a}_{\text{cloud}} - \boldsymbol{a}_{\text{ng}}\right) T^2$$

$$\frac{\Phi}{k_{\text{eff}} T^2} = \boldsymbol{e}_i \cdot \left(\boldsymbol{a}_{\text{cloud}} - \boldsymbol{a}_{\text{ng}}\right) = \boldsymbol{e}_i \cdot \boldsymbol{a}_{\text{cloud}} - \boldsymbol{e}_i \cdot \boldsymbol{a}_{\text{ng}}$$

$$\boldsymbol{e}_i \cdot \boldsymbol{a}_{\text{ng}} = -\frac{\Phi}{k_{\text{eff}} T^2} + \boldsymbol{e}_i \cdot \boldsymbol{a}_{\text{cloud}}$$

Replacing the acceleration of the atom cloud, which is given by Eq. (28), in the equation above, which results in Eq. (32):

$$\boldsymbol{e}_i \cdot \boldsymbol{a}_{\text{ng}} = -\frac{\Phi}{k_{\text{eff}} T^2} + \boldsymbol{e}_i \cdot \left(-\left(V - \Omega^2 - \dot{\Omega}\right)(\boldsymbol{r}_{\text{cloud}} - \boldsymbol{r}_{\text{CoM}}) + 2\boldsymbol{\omega} \times \boldsymbol{v}_{\text{cloud}}\right)$$

CAI gradiometer observation equation

From Eq. (59):

$$\frac{\Phi_{i,l}}{k_{\text{eff}} T^2} = \boldsymbol{e}_i \cdot \left(-\boldsymbol{a}_{\text{ng,l}} - \left(V - \Omega^2 - \dot{\Omega}\right)(\boldsymbol{r}_{\text{cloud,l}} - \boldsymbol{r}_{\text{CoM}}) + 2\boldsymbol{\omega} \times \boldsymbol{v}_{\text{cloud,l}}\right),$$

the phase measurement of cloud l is:

$$\Phi_{i,l} = k_{\text{eff}} T^2 \boldsymbol{e}_i \cdot \left(-\boldsymbol{a}_{\text{ng,l}} - \left(V - \Omega^2 - \dot{\Omega}\right)(\boldsymbol{r}_{\text{cloud,l}} - \boldsymbol{r}_{\text{CoM}}) + 2\boldsymbol{\omega} \times \boldsymbol{v}_{\text{cloud,l}}\right),$$

and the differential measurement $\delta\Phi_i$ is:

$$\delta\Phi_i \equiv \Phi_{i,1} - \Phi_{i,2} =$$
$$k_{\text{eff}} T^2 \boldsymbol{e}_i \cdot \left(-\boldsymbol{a}_{\text{ng,1}} - \left(V - \Omega^2 - \dot{\Omega}\right)(\boldsymbol{r}_{\text{cloud,1}} - \boldsymbol{r}_{\text{CoM}}) + 2\boldsymbol{\omega} \times \boldsymbol{v}_{\text{cloud,1}}\right) -$$
$$k_{\text{eff}} T^2 \boldsymbol{e}_i \cdot \left(-\boldsymbol{a}_{\text{ng,2}} - \left(V - \Omega^2 - \dot{\Omega}\right)(\boldsymbol{r}_{\text{cloud,2}} - \boldsymbol{r}_{\text{CoM}}) + 2\boldsymbol{\omega} \times \boldsymbol{v}_{\text{cloud,2}}\right)$$

If $\boldsymbol{r}$ is measured from the CoM, $\boldsymbol{v}_{\text{cloud,1}}$ and $\boldsymbol{v}_{\text{cloud,2}}$ are both given by $\boldsymbol{v}_{\text{cloud,therm}}$(assumed to be a random variable):

$$\frac{\delta\Phi_i}{k_{\text{eff}} T^2} = \boldsymbol{e}_i \cdot \left(-\boldsymbol{a}_{\text{ng,1}} + \boldsymbol{a}_{\text{ng,2}} - \left(V - \Omega^2 - \dot{\Omega}\right)\delta\boldsymbol{r}_{\text{cloud}} + 2\boldsymbol{\omega} \times \boldsymbol{v}_{\text{cloud,therm}}\right)$$

Since $\boldsymbol{a}_{\text{ng,1}} = \boldsymbol{a}_{\text{ng,2}}$ and $\delta\boldsymbol{r}_{\text{cloud}} = L_{\text{GG}} \boldsymbol{e}_i$, we arrive at Eq. (61):

$$\frac{\delta\Phi_i}{k_{\text{eff}} T^2} = \boldsymbol{e}_i \cdot \left(-\left(V - \Omega^2 - \dot{\Omega}\right) L_{\text{GG}} \boldsymbol{e}_i + 2\boldsymbol{\omega} \times \boldsymbol{v}_{\text{cloud,therm}}\right)$$

The scalar evaluation of this expression requires:

$$\boldsymbol{V}\boldsymbol{e}_i = \begin{bmatrix} V_{ii} \\ V_{ij} \\ V_{ik} \end{bmatrix} \text{ and } \boldsymbol{e}_i \cdot (\boldsymbol{V}\boldsymbol{e}_i) = V_{ii},$$

$$\Omega^2 \boldsymbol{e}_i = \begin{bmatrix} -\omega_j^2 - \omega_k^2 \\ \omega_i \omega_j \\ \omega_i \omega_k \end{bmatrix} \text{ and } \boldsymbol{e}_i \cdot \left(\Omega^2 \boldsymbol{e}_i\right) = -\omega_j^2 - \omega_k^2,$$

$$\dot{\Omega}\boldsymbol{e}_i = \begin{bmatrix} 0 \\ \dot{\omega}_k \\ \dot{\omega}_j \end{bmatrix} \text{ and } \boldsymbol{e}_i \cdot \left(\dot{\Omega}\boldsymbol{e}_i\right) = 0,$$

$$\boldsymbol{\omega} \times \boldsymbol{v} = \begin{bmatrix} \omega_j v_k - \omega_k v_j \\ \omega_k v_i - \omega_i v_k \\ \omega_i v_j - \omega_j v_i \end{bmatrix} \text{ and } \boldsymbol{e}_i \cdot (\boldsymbol{\omega} \times \boldsymbol{v}) = \omega_j v_k - \omega_k v_j,$$

resulting in:

$$\frac{\delta\Phi_i}{k_{\text{eff}} T^2} = -\left(V_{ii} + \omega_j^2 + \omega_k^2\right) L_{\text{GG}} + 2\omega_j v_{\text{cloud,therm},k} - 2\omega_k v_{\text{cloud,therm},j}$$

$$\frac{\delta\Phi_i}{k_{\text{eff}} T^2} \frac{1}{L_{\text{GG}}} = -V_{ii} - \omega_j^2 - \omega_k^2 + \frac{2}{L_{\text{GG}}} \omega_j v_{\text{cloud,therm},k} - \frac{2}{L_{\text{GG}}} \omega_k v_{\text{cloud,therm},j}$$

Rearranging, results in Eq. (62):

$$V_{ii} = -\frac{1}{L_{\text{GG}}} \frac{\delta\Phi_i}{k_{\text{eff}} T^2} - \omega_j^2 - \omega_k^2 + \frac{2}{L_{\text{GG}}} \left(\omega_j v_{\text{cloud,therm},k} - \omega_k v_{\text{cloud,therm},j}\right)$$

For a CAI gradiometer oriented along the other axes:

$$V_{jj} = -\frac{1}{L_{\text{GG}}} \frac{\delta\Phi_j}{k_{\text{eff}} T^2} - \omega_k^2 - \omega_i^2 + \frac{2}{L_{\text{GG}}} \left(\omega_k v_{\text{cloud,therm},i} - \omega_i v_{\text{cloud,therm},k}\right),$$

$$V_{kk} = -\frac{1}{L_{\text{GG}}} \frac{\delta\Phi_k}{k_{\text{eff}} T^2} - \omega_i^2 - \omega_j^2 + \frac{2}{L_{\text{GG}}} \left(\omega_i v_{\text{cloud,therm},j} - \omega_j v_{\text{cloud,therm},i}\right),$$

derived considering the following relations:

$\boldsymbol{e}_j \cdot \left(\boldsymbol{V}\boldsymbol{e}_j\right) = V_{jj}$ and $.\boldsymbol{e}_k \cdot (\boldsymbol{V}\boldsymbol{e}_k) = V_{kk}$

$\boldsymbol{e}_j \cdot \left(\Omega^2 \boldsymbol{e}_j\right) = -\omega_i^2 - \omega_k^2$ and $\boldsymbol{e}_k \cdot \left(\Omega^2 \boldsymbol{e}_k\right) = -\omega_i^2 - \omega_j^2$

$$\boldsymbol{e}_j \cdot \left(\dot{\Omega}\boldsymbol{e}_j\right) = \boldsymbol{e}_k \cdot \left(\dot{\Omega}\boldsymbol{e}_k\right) = 0$$

$$\boldsymbol{e}_j \cdot (\boldsymbol{\omega} \times \boldsymbol{v}) = \omega_k v_i - \omega_i v_k \text{ and } \boldsymbol{e}_k \cdot (\boldsymbol{\omega} \times \boldsymbol{v}) = \omega_i v_j - \omega_j v_i$$

Angular velocity signal magnitude

To assess the signal size of the angular velocity, we make several assumptions about the orbit and attitude control. First, we assume an orbit at an altitude of 500 km, which

yields an orbital period of $T_{\text{orb}} = 95min$. Next, we assume that the satellite is nadir pointing, which results in a mean pitch rate of:

$$\text{mean}(\omega_y) = 2\pi/T_{\text{orb}} = 1.1\,\text{mrad/s}. \tag{78}$$

Further, we assume that the satellite is pointing in the direction of the atmospheric flow to minimize the effects of drag. The direction of the flow relative to the satellite is composed of the inertial velocity of 7.6 km/s and the corotation of the atmosphere, which is 500 m/s at the equator in an eastward direction. The worst case is a polar orbit, in which the inertial velocity is perpendicular to the velocity of the corotating atmosphere. The maximum yaw angle at the equator is $\arcsin(0.5km/7.6km) = 3.77^{\circ}$. Since the velocity of the corotating atmosphere is zero at the pole, the yaw angle is also zero. Thus, the yaw angle changes from 3.77° to 0° during a quarter of an orbit, i.e., by $3.77^{\circ}/(T_{\text{orb}}/4) = 4.6 \times 10^{-5} rad/s$. To calculate the RMS of the angular velocity, we assume that the yaw angle varies like a sine function with an orbital period, i.e.:

$$\psi = 3.77^{\circ}\sin(2\pi t/T_{\text{orb}}). \tag{79}$$

The angular velocity is the time derivative of that function:

$$\omega_z = \frac{\partial\psi}{\partial t} = 3.77^{\circ}\,2\pi/T_{\text{orb}}\cos(2\pi t/T_{\text{orb}}). \tag{80}$$

The integral of the squared function is:

$$\begin{aligned}\int_0^{T_{orb}} \omega_z dt &= (3.77^{\circ}\,2\pi/T_{\text{orb}})^2 \int_0^{T_{orb}} \cos^2(2\pi t/T_{\text{orb}})dt \\ &= (3.77^{\circ}\,2\pi/T_{\text{orb}})^2 \tfrac{1}{2}\int_0^{T_{orb}} 1-\sin(4\pi t/T_{\text{orb}})dt \\ &= (3.77^{\circ}\,2\pi/T_{\text{orb}})^2 \tfrac{1}{2}[t - 4\pi/T_{orb}\cos(4\pi t/T_{\text{orb}})]_0^{T_{orb}} \\ &= (3.77^{\circ}\,2\pi/T_{\text{orb}})^2 T_{\text{orb}}/2.\end{aligned} \tag{81}$$

The RMS is then the square root of the integral divided by T_{orb}:

$$\begin{aligned}\text{RMS}(\omega_z) &= \sqrt{\frac{1}{T_{\text{orb}}}\int_0^{T_{\text{orb}}} \omega_z dt} = 3.77^{\circ}\frac{2\pi}{T_{\text{orb}}\sqrt{2}} \\ &= 5.1 \times 10^{-5}\,rad/s.\end{aligned} \tag{82}$$

When magnetic torquers are the only means for attitude control, there is typically no control of the roll at the equator because the magnetic field lines are parallel to the roll axis. With that in mind, we assume that the RMS of the roll rate is:

$$\text{RMS}(\omega_x) = 0.1\,\text{mrad/s}.$$

Non-gravitational acceleration signal magnitude

Some of the error propagations require assumptions about the size of the non-gravitational acceleration signal. Considering that aerodynamic accelerations are large at low altitudes, we use GOCE data as a worst-case scenario. Typical acceleration signal sizes are reported in Table 3.

The DFC of GOCE was estimated to reduce non-gravitation accelerations down to 1nm/s^2 (Christophe et al., 2018; Visser and van den IJssel, 2016). As such, the assumptions on 1D and 3D DFC shown in Table 3 are conservative.

Gravity gradient signal magnitude

Assuming a LEO orbit, the signal amplitude of the (symmetric) gravity gradient tensor in the Local Horizontal Reference Frame (LHRF) $V^{(}\text{LHRF})$ at 450 km altitude is (e.g. Rosen, 2021):

$$\text{RMS}(V^{(}\text{LHRF})) \approx \begin{bmatrix} 1200 & 0 & 0 \\ & 1200 & 0 \\ & & -2400 \end{bmatrix} + \begin{bmatrix} 3.01 & 0.03 & 0.09 \\ 4.22 & 4.38 & \\ -7.23 & & \end{bmatrix} [E]. \tag{83}$$

The first term is associated with the signal caused by the central term of the gravity field, and the static gravity field of the Earth causes the second term. We ignored the term caused by the temporal variations of the gravity field.

Reference frames

Earth-centred, Earth-fixed reference frame

The ECEF reference frame, also known as Terrestrial Reference Frame (TRF), Earth Centred Fixed reference frame (ECF), Conventional Terrestrial Frame (CTF) and Earth-Fixed Reference Frame (EFRF), is centred at the COM of the Earth. The x-axis points towards longitude 0 degrees and is parallel to the equatorial plane. The y-axis, also parallel to the equatorial plane, points towards 90 degrees longitude. The z-axis points towards the North pole. The TRF is suitable for representing geophysical processes in the Earth system.

Earth-centred, inertial reference frame

The ECI reference frame, also know as Celestial Reference Frame (CRF), Conventional Inertial Frame (CIF) and Inertial Reference Frame (IRF), is the quasi-inertial reference frame defined with the x-axis pointing towards the direction of the mean equinox at J2000.0 epoch (noon on 1st of January 2000, Terrestrial Time), the z-axis points to the North pole at that epoch (formally, orthogonal to the plane defined by the mean equator at J2000.0) and the y-axis closes the right-handed set of orthogonal axes. The origin of the CRF is located at the COM of the Earth. The quasi-inertial property of this reference frame makes it suitable to represent the motion of a spacecraft.

Satellite reference frame

The SRF is used to define the spacecraft's geometry. The axes are connected to the body of the spacecraft in a predefined (but otherwise arbitrary) way. The attitude determi-

Table 3
Non-gravitational signal size in nm/s^2, mean for long-track and standard deviation for cross-track and radial directions, for the case of the GOCE mission, considering 1D and (hypothetical) 3D drag control.

[nm/s^2]	GOCE 230 km	1D Drag Control	3D Drag Control
Along-track (mean)	10,000	10	10
Cross-track (STD)	289	289	10
Radial (STD)	22	22	10

nation system provides measurements that connect the inertial to this reference frame. The pressure forces due to Solar and Earth radiation, as well as those of aerodynamic nature, are most suitably defined in this reference frame since the orientation of the satellite exterior panels is constant. This reference frame also serves as a basis for defining the reference frames of the various sensors and actuators on board the satellites, such as the accelerometer(s), the startracker(s), magneto-torquers, propulsion systems, etc.

Local Horizontal reference frame

The LHRF is centred at the CoM of the orbiting satellite. The z −axis is parallel to the radial direction and points away from the CoM of the Earth. The x -axis is perpendicular to the z-axis and points in the direction of geographic North. The y-axis, also perpendicular to the z-axis, points towards the West. This reference frame is preferred to represent the physical forces acting on the satellite, particularly the gravitational force.

Error in reconstructing the centrifugal accelerations in ll-SST

The errors in reconstructing the centrifugal accelerations are given by (Ditmar et al., 2012):

$$s_c = -\frac{2v_z}{\rho}s_{v_z} + \frac{v_z^2}{\rho^2}s_\rho \approx -2\sqrt{\frac{GM}{R_{\text{orb}}^3}}s_{v_z} + \frac{GM}{R_{\text{orb}}^3}s_\rho \tag{84}$$

with Earth's gravitational parameter GM is $3.986 \times 10^{14}\text{m}^3/\text{s}^2$ and R_{orb} is 6.897×10^6m, which is related to an orbital period of 95 min, or 525.7 km altitude. The assumption for R_{orb} is relatively arbitrary for LEO, since the factor GM/R_{orb}^3 only increases by 15.3 % when the altitude decreases to 182 km.

One option to derive representative amplitude and spectra of the errors in the radial velocity v_z is to compute the difference between 1) the inter-satellite velocities computed from orbit integration and 2) the GRACE's KBR data. This was done for January, February, July, August, and September of 2006, with a total of over 6 billion data points (Teixeira da Encarnação, 2015). This analysis removed data that had low SNR, surrounding gaps resulting from phase breaks, discontinuities in the integrated orbit arcs (every 6 h) and outliers, which were removed iteratively when larger than 4-σ, until changes in the standard deviations (STD) of the remaining data did not change significantly.

The data considered in the analysis revealed an STD of 2.19 μm/s, which is close to the 4 μm/s that Ditmar et al. (2012) considered in their study, when a less strict data preprocessing scheme was considered.

Importantly, we assume in this study that the spectra of these errors are a simplified representation of the results in Fig. 6.3 of Teixeira da Encarnação (2015), as shown in Fig. 20 and reported numerically in Table 4.

We further consider that the velocity errors along the LoS direction are representative in magnitude and spectra of the radial velocity errors, which are relevant to computing the error in reconstructing the centrifugal accelerations. It is important to have a good estimate of the spectra of radial velocity errors; for example, if white noise is considered, their propagation to the range-acceleration space would incorrectly magnify the high frequencies.

Considering the error magnitude s_ρ for both KBR and LRI ranging instruments, as well as the SuperSTAR accelerometers (cf. Section 2.2), Fig. 21 contextualizes the amplitude of s_c for GRACE-FO.

The errors in reconstructing the centrifugal accelerations (light blue line) are not dominant over the entire frequency band, which is expected because this error type is not reported in the literature as detrimental to the quality of the estimated gravity field models. the use of variational

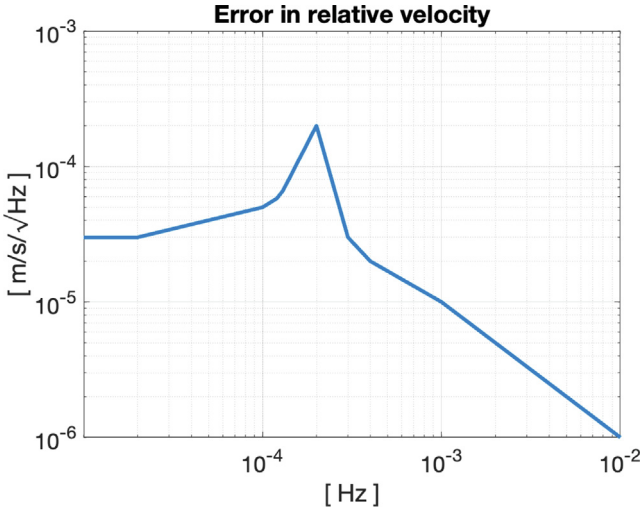

Fig. 20. Errors in the relative velocity, estimated from the difference between KBR data and the distance computed from integrated orbits.

Table 4
Numerical values of the assumed amplitude spectra of the radial velocity errors.

Frequency [mHz]	0.01	0.02	0.1	0.125	0.2	0.3	0.4	1	10
Amplitude [m/s/$\sqrt{\text{Hz}}$]	3×10^{-5}	3×10^{-5}	5×10^{-5}	6×10^{-5}	2×10^{-4}	3×10^{-5}	2×10^{-5}	1×10^{-5}	1×10^{-5}

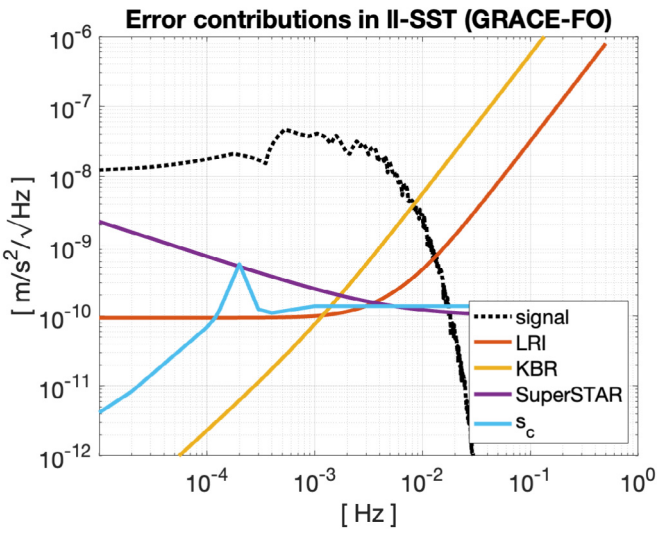

Fig. 21. Error amplitude spectra for GRACE-FO's LRI (red line), KBR (yellow line), ranging instruments, the SuperSTAR accelerometer (purple line), and the error in reconstructing the centrifugal accelerations (blue line), compared to the estimated time-variable signal magnitude (dotted black line).

equations as the gravity field estimation approach is an effective way to mitigate its effect (Weigelt, 2017).

It should be noted that the component related to the accuracy of the radial velocity s_{v_z} is, by far, the dominant term in Eq. (84). Consequently, s_c is intrinsic to the ll-SST concept that uses the leader/follower formation (also known as *trailing* or *inline*) and has the reported magnitude irrespective of the ISR and accelerometer accuracies.

Methodology for selection of CAI parameters

Our objective is to identify instrument configurations that deliver acceleration sensitivity suitable for low-low SST missions while remaining technically plausible for a flight implementation. To achieve this, we coupled a physics-based performance model with a set of empirically derived cost proxies that penalize design choices that, in the authors' experience, drive mass, volume, complexity, and therefore program risk. The section below summarizes the two building blocks of trade-space exploration and how they are combined.

Performance metric

CAI noise is dominated by quantum-projection (shot) noise in the measurement of the transition probability. Assuming technical noise is kept subdominant, we can use Eq. (20) to calculate the performance in terms of acceleration sensitivity. We also use this equation to define the levers available to the instrument designer: longer interferometer time, larger momentum transfer, more atoms, and stronger entanglement all lower the noise floor, but each lever has engineering consequences that quickly become mission-limiting in a spaceborne context.

Engineering cost proxies

Four parameters were selected as the dominant cost drivers:

The chamber height H is evaluated from the cloud's ballistic half-excursion vT; for the Rb^{87} Raman, this gives $v \approx 3\beta$ mm/s.

Each proxy is mapped to a dimensionless cost coefficient:

$$C = \frac{e^{qx} - 1}{e^{qx_{\max}} - 1}, \tag{85}$$

which monotonically scales from 0 at the reference value ($x = 0$) to 1 at an upper admissible bound $x_{\max}$. The shaping factor q allows us to encode how abruptly cost is believed to rise as the limit is approached; steep curves (large q)

Table 5
Cost drivers and proxy variables.

Symbol	Physical lever	Rationale for penalising	Proxy variable x	Shaping Factor q	Weight w
T	Pulse-separation time	System isolation, mechanical and optical stability	$T(s)$	0.01	0.1
N	Atom number	Laser power & linewidth, cooling/launch duty-cycle, vacuum quality, trap quality	$\log_{10} N$	1	1
α	Entanglement degree	control systems, sensitivity to decoherence, high-finesse optics	α	2	5
H	Chamber height	Structural mass, magnetic shielding, field homogeneity, alignment precision, satellite real estate	$H = vT$ with $v = \frac{\beta}{2}\frac{\hbar k}{m}$	10	10

mimic "cliff edges" in manufacturability, while shallow curves reflect gradual cost growth.

Finally, subjective weights w_i convert the individual coefficients into a composite score

$$C_{\text{total}} = \sum_i w_i C_i, \tag{86}$$

The large weight on vacuum-chamber height echoes launch-vehicle and thus satellite volume constraints and centre-of-mass offsets that quickly dominate spacecraft design. Entanglement complexity is also strongly penalised because only modest levels of spin-squeezing have yet been demonstrated with a moderate number of atoms (Greve et al., 2022).

Trade-space exploration

For a grid of (β, T, N, α), we compute the sensitivity $s^{(s2s)}_{\text{CAI,ng}}$ and total cost as shown above. Parameter combinations that satisfy a notional noise requirement are plotted in cost–performance space and ranked by increasing cost, providing a means to identify configurations that offer relatively favorable trade-offs. The resulting distribution of design points is illustrated in Fig. 8 with sensitivity on the x-axis and cost on the y-axis, where each point represents a distinct parameter set.

The purpose of this approach is not to prescribe an optimal instrument design, but to establish a transparent and adaptable framework for exploring the first-order trade-space. The performance model and cost functions are constructed to be analytically simple and empirically tunable, allowing for updates as new experimental results and system-level constraints emerge. In this way, the methodology facilitates early-stage assessment of design trends and sensitivities, supporting the iterative development of CAI concepts for spaceborne gravity missions.

References

Abend, S., Allard, B., Arnold, A.S., Ban, T., Barry, L., Battelier, B., Bawamia, A., Beaufils, Q., Bernon, S., Bertoldi, A., Bonnin, A., Bouyer, P., Bresson, A., Burrow, O.S., Canuel, B., Desruelle, B., Drougakis, G., Forsberg, R., Gaaloul, N., Gauguet, A., Gersemann, M., Griffin, P.F., Heine, H., Henderson, V.A., Herr, W., Kanthak, S., Krutzik, M., Lachmann, M.D., Lammegger, R., Magnes, W., Mileti, G., Mitchell, M.W., Mottini, S., Papazoglou, D., Pereira Dos Santos, F., Peters, A., Rasel, E., Riis, E., Schubert, C., Seidel, S.T., Tino, G. M., Van Den Bossche, M., Von Klitzing, W., Wicht, A., Witkowski, M., Zahzam, N., Zawada, M., 2023. Technology roadmap for cold-atoms based quantum inertial sensor in space. AVS Quantum Sci. 5. https://doi.org/10.1116/5.0098119.

Abich, K., Abramovici, A., Amparan, B., Baatzsch, A., Okihiro, B.B., Barr, D.C., Bize, M.P., Bogan, C., Braxmaier, C., Burke, M.J., Clark, K.C., Dahl, C., Dahl, K., Danzmann, K., Davis, M.A., de Vine, G., Dickson, J.A., Dubovitsky, S., Eckardt, A., Ester, T., Barranco, G.F., Flatscher, R., Flechtner, F., Folkner, W.M., Francis, S., Gilbert, M.S., Gilles, F., Gohlke, M., Grossard, N., Guenther, B., Hager, P., Hauden, J., Heine, F., Heinzel, G., Herding, M., Hinz, M., Howell, J., Katsumura, M., Kaufer, M., Klipstein, W., Koch, A., Kruger, M., Larsen, K., Lebeda, A., Lebeda, A., Leikert, T., Liebe, C.C., Liu, J., Lobmeyer, L., Mahrdt, C., Mangoldt, T., McKenzie, K., Misfeldt, M., Morton, P.R., Müller, V., Murray, A.T., Nguyen, D.J., Nicklaus, K., Pierce, R., Ravich, J.A., Reavis, G., Reiche, J., Sanjuan, J., Schütze, D., Seiter, C., Shaddock, D., Sheard, B., Sileo, M., Spero, R., Spiers, G., Stede, G., Stephens, M., Sutton, A., Trinh, J., Voss, K., Wang, D., Wang, R.T., Ware, B., Wegener, H., Windisch, S., Woodruff, C., Zender, B., Zimmermann, M., 2019. In-orbit performance of the GRACE follow-on laser ranging interferometer. Phys. Rev. Lett. 123, 31101. https://doi.org/10.1103/PhysRevLett.123.031101.

Abrykosov, P., Pail, R., Gruber, T., Zahzam, N., Bresson, A., Hardy, E., Christophe, B., Bidel, Y., Carraz, O., Siemes, C., 2019. Impact of a novel hybrid accelerometer on satellite gravimetry performance. Adv. Space Res. 63, 3235–3248. https://doi.org/10.1016/j.asr.2019.01.034.

Airbus, 2022. ASTRIX® 200 specification sheet. Airbus.

Allasio, A., Anselmi, A., Catastini, G., Cesare, S., Dumontel, M., Saponara, M., Sechi, G., Tramutola, A., Vinai, B., André, G., Fehringer, M., Muzi, D., 2010. Goce mission: design phases and in-flight experiences. Adv. Astronaut. Sci., 627–646

Amri, S., 2022. Optimized matter-wave lensing of quantum gases for precision atom sensors. Université Paris-Saclay.

Barrett, B., Cheiney, P., Battelier, B., Napolitano, F., Bouyer, P., 2019. Multidimensional atom optics and interferometry. Phys. Rev. Lett. 122. https://doi.org/10.1103/physrevlett.122.043604.

Beaufils, Q., Lefebve, J., Baptista, J.G., Piccon, R., Cambier, V., Sidorenkov, L.A., Fallet, C., Lévèque, T., Merlet, S., Pereira Dos Santos, F., 2023. Rotation related systematic effects in a cold atom interferometer onboard a nadir pointing satellite. npj Microgravity 9, 53. https://doi.org/10.1038/s41526-023-00297-w.

Becker, D., Lachmann, M.D., Seidel, S.T., Ahlers, H., Dinkelaker, A.N., Grosse, J., Hellmig, O., Müntinga, H., Schkolnik, V., Wendrich, T., Wenzlawski, A., Weps, B., Corgier, R., Franz, T., Gaaloul, N., Herr, W., Lüdtke, D., Popp, M., Amri, S., Duncker, H., Erbe, M., Kohfeldt, A., Kubelka-Lange, A., Braxmaier, C., Charron, E., Ertmer, W., Krutzik, M., Lämmerzahl, C., Peters, A., Schleich, W.P., Sengstock, K., Walser, R., Wicht, A., Windpassinger, P., Rasel, E.M., 2018. Space-borne bose–einstein condensation for precision interferometry. Nature 562, 391–395. https://doi.org/10.1038/s41586-018-0605-1.

Belenchia, A., Carlesso, M., Bayraktar, Ö., Dequal, D., Derkach, I., Gasbarri, G., Herr, W., Li, Y.L., Rademacher, M., Sidhu, J., Oi, D.K. L., Seidel, S.T., Kaltenbaek, R., Marquardt, C., Ulbricht, H., Usenko, V.C., Wörner, L., Xuereb, A., Paternostro, M., Bassi, A., 2022. Quantum physics in space. Phys. Rep. 951, 1–70. https://doi.org/10.1016/j.physrep.2021.11.004.

Benyoucef, M., 2025. Recent advances in photonic quantum technologies. Adv. Quantum Technol. 8. https://doi.org/10.1002/qute.202400628.

Carraz, O., Siemes, C., Massotti, L., Haagmans, R., Silvestrin, P., 2014. A spaceborne gravity gradiometer concept based on cold atom interferometers for measuring earth's gravity field. Microgravity Sci. Technol. 26, 139–145. https://doi.org/10.1007/s12217-014-9385-x.

Cesare, S., Dionisio, S., Saponara, M., Bravo-Berguño, D., Massotti, L., Teixeira da Encarnação, J., Christophe, B., 2022. Drag and attitude control for the next generation gravity mission. Remote Sens. 14, 2916. https://doi.org/10.3390/rs14122916.

Cheng, M., Ries, J., 2017. The unexpected signal in GRACE estimates of C20. J. Geod. 91, 897–914. https://doi.org/10.1007/s00190-016-0995-5.

Christophe, B., Boulanger, D., Foulon, B., Huynh, P.-A., Lebat, V., Liorzou, F., Perrot, E., 2015. A new generation of ultra-sensitive electrostatic accelerometers for GRACE follow-on and towards the next generation gravity missions. Acta Astronaut. 117, 1–7. https://doi.org/10.1016/j.actaastro.2015.06.021.

Christophe, B., Foulon, B., Liorzou, F., Lebat, V., Boulanger, D., Huynh, P.-A., Zahzam, N., Bidel, Y., Bresson, A., 2018. Status of development of the future accelerometers for next generation gravity missions. Int. Assoc. Geod. Symposia., 85–89 https://doi.org/10.1007/1345_2018_42.

Dahl, K., Cebeci, P., Fitzau, O., Giesberts, M., Greve, C., Krutzik, M., Peters, A., Amairi Pyka, S., Sanjuan, J., Schiemangk, M., Schuldt, T., Voss, K., Wicht, A., 2019. A new laser technology for LISA. In: Karafolas, N., Sodnik, Z., Cugny, B. (Eds.), International Conference on Space Optics — ICSO 2018. SPIE, p. 11. https://doi.org/10.1117/12.2535931.

Ditmar, P., Teixeira da Encarnação, J., Hashemi Farahani, H., 2012. Understanding data noise in gravity field recovery on the basis of inter-satellite ranging measurements acquired by the satellite gravimetry mission GRACE. J. Geod. 86, 441–465. https://doi.org/10.1007/s00190-011-0531-6.

Dobslaw, H., Bergmann-Wolf, I., Forootan, E., Dahle, C., Mayer-Gürr, T., Kusche, J., Flechtner, F., 2016. Modeling of present-day atmosphere and ocean non-tidal de-aliasing errors for future gravity mission simulations. J. Geod. 90, 423–436. https://doi.org/10.1007/s00190-015-0884-3.

Douch, K., Wu, H., Schubert, C., Müller, J., Pereira dos Santos, F., 2018. Simulation-based evaluation of a cold atom interferometry gradiometer concept for gravity field recovery. Adv. Space Res. 61, 1307–1323. https://doi.org/10.1016/j.asr.2017.12.005.

Ghobadi-Far, K., Han, S.-C., Loomis, B.D., Luthcke, S.B., 2018. On computation of potential, gravity and gravity gradient from GRACE inter-satellite ranging data: a systematic study. Springer, Berlin, Heidelberg, pp. 1–6.

Goswami, S., Francis, S.P., Bandikova, T., Spero, R.E., 2021. Analysis of GRACE follow-on laser ranging interferometer derived inter-satellite pointing angles. IEEE Sensors J. 21, 19209–19221. https://doi.org/10.1109/JSEN.2021.3090790.

Greve, G.P., Luo, C., Wu, B., Thompson, J.K., 2022. Entanglement-enhanced matter-wave interferometry in a high-finesse cavity. Nature 610, 472–477. https://doi.org/10.1038/s41586-022-05197-9.

Groh, A., Horwath, M., Horvath, A., Meister, R., Sørensen, L.S., Barletta, V.R., Forsberg, R., Wouters, B., Ditmar, P., Ran, J., Klees, R., Su, X., Shang, K., Guo, J., Shum, C.K., Schrama, E., Shepherd, A., 2019. Evaluating GRACE mass change time series for the antarctic and Greenland ice sheet—methods and results. Geosciences 9, 415. https://doi.org/10.3390/geosciences9100415.

Gross, C., 2012. Spin squeezing, entanglement and quantum metrology with bose–einstein condensates. J. Phys. B: At. Mol. Opt. Phys. 45. https://doi.org/10.1088/0953-4075/45/10/103001 103001.

Han, S.-C., 2006. Crustal dilatation observed by GRACE after the 2004 sumatra-andaman earthquake. Science 313, 658–662. https://doi.org/10.1126/science.1128661.

Helleputte, T.V., Doornbos, E., Visser, P., 2009. CHAMP and GRACE accelerometer calibration by GPS-based orbit determination. Adv. Space Res. 43, 1890–1896. https://doi.org/10.1016/j.asr.2009.02.017.

Heller-Kaikov, B., Pail, R., Daras, I., 2023. Mission design aspects for the mass change and geoscience international constellation (MAGIC). Geophys. J. Int. 235, 718–735. https://doi.org/10.1093/gji/ggad266.

Herceg, M., Jørgensen, P.S., Jørgensen, J.L., 2017. Characterization and compensation of thermo-elastic instability of SWARM optical bench on micro advanced stellar compass attitude observations. Acta Astronaut. 137, 205–213. https://doi.org/10.1016/j.actaastro.2017.04.018.

HosseiniArani, A., Schilling, M., Tennstedt, B., Kupriyanov, A., Beaufils, Q., Knabe, A., Sreekantaiah, A.C., Pereira Dos Santos, F., Schön, S., Müller, J., 2025. Combined classical and quantum accelerometers for future satellite gravity missions. Earth Space Sci. 12. https://doi.org/10.1029/2024EA004187 e2024EA004187.

Jiang, D., Wang, J., Huang, Y., Zhou, K., Ding, X., Fu, J., 2014. The review of GRACE data applications in terrestrial hydrology monitoring. Adv. Meteorol. 2014, 1–9. https://doi.org/10.1155/2014/725131.

Kaczmarczuk, B., Baptista, J.G., Merlet, S., Sidorenkov, L.A., Beaufils, Q., Dos Santos, F.P., 2025. Statistical analysis of the rotation induced decay of the contrast in an onboard atom interferometer. IEEE Sensors J. 1–1. https://doi.org/10.1109/jsen.2025.3586409.

Kaltenbaek, R., Acin, A., Bacsardi, L., Bianco, P., Bouyer, P., Diamanti, E., Marquardt, C., Omar, Y., Pruneri, V., Rasel, E., Sang, B., Seidel, S., Ulbricht, H., Ursin, R., Villoresi, P., van den Bossche, M., von Klitzing, W., Zbinden, H., Paternostro, M., Bassi, A., 2021. Quantum technologies in space. Exp. Astron. 51, 1677–1694. https://doi.org/10.1007/s10686-021-09731-x.

Knabe, A., Schilling, M., Wu, H., HosseiniArani, A., Müller, J., Beaufils, Q., dos Santos, F.P., 2022. The benefit of accelerometers based on cold atom interferometry for future satellite gravity missions. Int. Assoc. Geod. Symposia., 213–220 https://doi.org/10.1007/1345_2022_151.

Kornfeld, R.P., Arnold, B.W., Gross, M.A., Dahya, N.T., Klipstein, W. M., Gath, P.F., Bettadpur, S., 2019. GRACE-FO: the gravity recovery and climate experiment follow-on mission. J. Spacecr. Rockets 56, 931–951. https://doi.org/10.2514/1.A34326.

Lévèque, T., Gauguet, A., Michaud, F., Pereira Dos Santos, F., Landragin, A., 2009. Enhancing the area of a raman atom interferometer using a versatile double-diffraction technique. Phys. Rev. Lett. 103, 80405. https://doi.org/10.1103/PhysRevLett.103.080405.

Lévèque, T., Fallet, C., Lefebve, J., Piquereau, A., Gauguet, A., Battelier, B., Bouyer, P., Gaaloul, N., Lachmann, M., Piest, B., Rasel, E., Müller, J., Schubert, C., Beaufils, Q., Pereira Dos Santos, F., 2023. CARIOQA: definition of a quantum pathfinder mission. In: Minoglou, K., Karafolas, N., Cugny, B. (Eds.), International Conference on Space Optics — ICSO 2022. Presented at the International Conference on Space Optics — ICSO 2022, p. 129. https://doi.org/10.1117/12.2690536.

Li, J., Chen, X., Zhang, D., Wang, W., Zhou, Y., He, M., Fang, J., Zhou, L., He, C., Jiang, J., Sun, H., Chen, Q., Qin, L., Li, X., Wang, Y., Zhang, X., Zhong, J., Li, R., An, M., Zhang, L., Wang, S., Li, Z., Wang, J., Zhan, M., 2025. Realization of a cold atom gyroscope in space. Natl. Sci. Rev. 12. https://doi.org/10.1093/nsr/nwaf012.

Luthcke, S.B., Saif, B., Fisher, K., Baird, L.R., Loomis, B., Everett, D., Banting, R., Piepmeier, J., Shappirio, M., Rowlands, D., 2021. Atom interferometer gravity gradiometer tech development readiness and performance. NASA Goddard Space Flight Center, Greenbelt, MD.

Malossi, N., Bodart, Q., Merlet, S., Lévèque, T., Landragin, A., Santos, F. P.D., 2010. Double diffraction in an atomic gravimeter. Phys. Rev. A 81, 13617. https://doi.org/10.1103/PhysRevA.81.013617.

Massotti, L., Siemes, C., March, G., Haagmans, R., Silvestrin, P., 2021. Next generation gravity mission elements of the mass change and geoscience international constellation: from orbit selection to instrument and mission design. Remote Sens. 13, 3935. https://doi.org/10.3390/rs13193935.

Migliaccio, F., Reguzzoni, M., Batsukh, K., Tino, G.M., Rosi, G., Sorrentino, F., Braitenberg, C., Pivetta, T., Barbolla, D.F., Zoffoli, S., 2019. MOCASS: a satellite mission concept using cold atom interferometry for measuring the Earth gravity field. Surv. Geophys. 40, 1029–1053. https://doi.org/10.1007/s10712-019-09566-4.

Mu, Q., Müller, J., Wu, H., Knabe, A., Zhong, M., 2024. Satellite gradiometry based on a new generation of accelerometers and its potential contribution to Earth gravity field determination. Adv. Space Res. 73, 3321–3344. https://doi.org/10.1016/j.asr.2023.08.023.

Müntinga, H., Ahlers, H., Krutzik, M., Wenzlawski, A., Arnold, S., Becker, D., Bongs, K., Dittus, H., Duncker, H., Gaaloul, N., Gherasim, C., Giese, E., Grzeschik, C., Hänsch, T.W., Hellmig, O., Herr, W., Herrmann, S., Kajari, E., Kleinert, S., Lämmerzahl, C., Lewoczko-Adamczyk, W., Malcolm, J., Meyer, N., Nolte, R., Peters, A., Popp, M., Reichel, J., Roura, A., Rudolph, J., Schiemangk, M., Schneider, M., Seidel, S.T., Sengstock, K., Tamma, V., Valenzuela, T., Vogel, A., Walser, R., Wendrich, T., Windpassinger, P., Zeller, W., Van Zoest, T., Ertmer, W., Schleich, W.P., Rasel, E.M., 2013. Interferometry with bose-einstein condensates in microgravity. Phys. Rev. Lett. 110, 93602. https://doi.org/10.1103/PhysRevLett.110.093602.

Peters, A., Chung, K., Chu, S., Francisco, S., 1999. Measurement of gravitational acceleration by dropping atoms. Nature 400, 849–852. https://doi.org/10.1038/23655.

Reubelt, T., Sneeuw, N., Pour, S.I., Hirth, M., Fichter, W., Müller, J., Brieden, P., Flechtner, F., Raimondo, J.-C., Kusche, J., Elsaka, B., Gruber, T., Pail, R., Murböck, M., Doll, B., Sand, R., Wang, X., Klein, V., Lezius, M., Danzmann, K., Heinzel, G., Sheard, B., Rasel, E., Gilowski, M., Schubert, C., Schäfer, W., Rathke, A., Dittus, H., Pelivan, I., 2014. Future gravity field satellite missions. In: Flechtner, F., Sneeuw, N., Schuh, W.-D. (Eds.), Observation of the System Earth from Space - CHAMP, GRACE, GOCE and Future Missions.

Springer Berlin Heidelberg, pp. 165–230. https://doi.org/10.1007/978-3-642-32135-1_21.

Romeshkani, M., Müller, J., Knabe, A., Schilling, M., 2025. Quantum gravimetry for future satellite gradiometry. Adv. Space Res. 75, 1653–1664. https://doi.org/10.1016/j.asr.2024.11.072.

Rosen, M.D., 2021. Analysis of hybrid satellite-to-satellite tracking and quantum gravity gradiometry architecture for time-variable gravity sensing missions. University of Texas at Austin. https://doi.org/10.26153/tsw/14541.

Rudolph, J., Herr, W., Grzeschik, C., Sternke, T., Grote, A., Popp, M., Becker, D., Müntinga, H., Ahlers, H., Peters, A., Lämmerzahl, C., Sengstock, K., Gaaloul, N., Ertmer, W., Rasel, E.M., 2015. A high-flux BEC source for mobile atom interferometers. New J. Phys. 17, 65001. https://doi.org/10.1088/1367-2630/17/6/065001.

Rummel, R., Yi, W., Stummer, C., 2011. GOCE gravitational gradiometry. J. Geod. 85, 777–790. https://doi.org/10.1007/s00190-011-0500-0.

Schütze, D., Stede, G., Müller, V., Gerberding, O., Mahrdt, C., Sheard, B., Heinzel, G., Danzmann, K., 2013. LISA-like laser ranging for GRACE follow-on. Astron. Soc. Pac. Conf. Proc. 467, 285–290.

Sheard, B.S., Heinzel, G., Danzmann, K., Shaddock, D.A., Klipstein, W. M., Folkner, W.M., 2012. Intersatellite laser ranging instrument for the GRACE follow-on mission. J. Geod. 86, 1083–1095. https://doi.org/10.1007/s00190-012-0566-3.

Siemes, C., Rexer, M., Haagmans, R., 2019. GOCE star tracker attitude quaternion calibration and combination. Adv. Space Res. 63, 1133–1146. https://doi.org/10.1016/j.asr.2018.10.030.

Sorrentino, F., Bongs, K., Bouyer, P., Cacciapuoti, L., De Angelis, M., Dittus, H., Ertmer, W., Giorgini, A., Hartwig, J., Hauth, M., Herrmann, S., Inguscio, M., Kajari, E., Könemann, T.T., Lämmerzahl, C., Landragin, A., Modugno, G., Pereira Dos Santos, F., Peters, A., Prevedelli, M., Rasel, E.M., Schleich, W.P., Schmidt, M., Senger, A., Sengstock, K., Stern, G., Tino, G.M., Walser, R., Angelis, M.D., Dittus, H., Ertmer, W., Giorgini, A., Hartwig, J., Hauth, M., Herrmann, S., Inguscio, M., Kajari, E., Könemann, T.T., Lämmerzahl, C., Landragin, A., Modugno, G., Pereira Dos Santos, F., Peters, A., Prevedelli, M., Rasel, E.M., Schleich, W.P., Schmidt, M., Senger, A., Sengstock, K., Stern, G., Tino, G.M., Walser, R., Matthias, J.H., Sven, H., Massimo, H., Endre, I., Könemann, T.T., Lämmerzahl, C., Landragin, A., Modugno, G., Pereira, F., Peters, A., Prevedelli, M., Rasel, E.M., Schleich, W.P., Schmidt, M., Senger, A., Sengstock, K., Stern, G., Maria, G., Reinhold, T., 2010. A compact atom interferometer for future space missions. Microgravity Sci. Technol. 22, 551–561. https://doi.org/10.1007/s12217-010-9240-7.

Sorrentino, F., Bodart, Q., Cacciapuoti, L., Lien, Y.-H., Prevedelli, M., Rosi, G., Salvi, L., Tino, G.M., 2014. Sensitivity limits of a raman atom interferometer as a gravity gradiometer. Phys. Rev. A 89, 23607. https://doi.org/10.1103/PhysRevA.89.023607.

Stedman, G.E., Schreiber, K.U., Bilger, H.R., 2003. On the detectability of the lense–thirring field from rotating laboratory masses using ring laser gyroscope interferometers. Class. Quantum Grav. 20, 2527–2540. https://doi.org/10.1088/0264-9381/20/13/305.

Steiger, C., Mardle, N., Emanuelli, P.P., 2014. GOCE end-of-mission operations report. ESA.

Stray, B., Bosch-Lluis, X., Thompson, R., Okino, C., Yu, N., Lay, N., Muirhead, B., Hyon, J., Leopardi, H., Brereton, P., Mylapore, A., Loomis, B., Luthcke, S., Ghuman, P., Bettadpur, S., Lachmann, M. D., Stolz, T., Kuehl, C., Weise, D., Ahlers, H., Schubert, C., Bawamia, A., Chiow, S., 2025. Quantum gravity gradiometry for future mass change science. EPJ Quantum Technol. 12, 35. https://doi.org/10.1140/epjqt/s40507-025-00338-1.

Szigeti, S.S., Hosten, O., Haine, S.A., 2021. Improving cold-atom sensors with quantum entanglement: prospects and challenges. Appl. Phys. Lett. 118. https://doi.org/10.1063/5.0050235 140501.

Teixeira da Encarnação, J., 2015. Next-generation satellite gravimetry for measuring mass transport in the Earth system. Delft University of Technology. https://doi.org/10.4233/uuid:d0c61fd2-804b-4827-ae8a-e0e93d282a56.

Touboul, P., Métris, G., Sélig, H., Le Traon, O., Bresson, A., Zahzam, N., Christophe, B., Rodrigues, M., 2016. Gravitation and geodesy with inertial sensors, from ground to spac. Aerosp. Lab J. 1–16. https://doi.org/10.12762/2016.AL12-11.

Travagnin, M., 2020. In: Cold Atom Interferometry for Earth Observation. Publications Office of the European Union, Luxembourg. https://doi.org/10.2760/225071.

Trimeche, A., Battelier, B., Becker, D., Bertoldi, A., Bouyer, P., Braxmaier, C., Charron, E., Corgier, R., Cornelius, M., Douch, K., Gaaloul, N., Herrmann, S., Müller, J., Rasel, E., Schubert, C., Wu, H., dos Santos, F.P., Pereira dos Santos, F., 2019. Concept study and preliminary design of a cold atom interferometer for space gravity gradiometry. Class. Quantum Grav. 36. https://doi.org/10.1088/1361-6382/ab4548 215004.

Visser, P.N.A.M.M., van den IJssel, J.A.A., 2016. Calibration and validation of individual GOCE accelerometers by precise orbit determination. J. Geod. 90, 1–13. https://doi.org/10.1007/s00190-015-0850-0.

Visser, P.N.A.M., van den IJssel, J.A., 2016. Orbit determination and estimation of non-gravitational accelerations for the GOCE reentry phase. Adv. Space Res. 58, 1840–1853. https://doi.org/10.1016/j.asr.2016.07.013.

Weigelt, M., 2017. The acceleration approach. pp. 97–126. https://doi.org/10.1007/978-3-319-49941-3_4.

Zahzam, N., Christophe, B., Lebat, V., Hardy, E., Huynh, P.-A., Marquet, N., Blanchard, C., Bidel, Y., Bresson, A., Abrykosov, P., Gruber, T., Pail, R., Daras, I., Carraz, O., 2022. Hybrid electrostatic-atomic accelerometer for future space gravity missions. Remote Sens. 14, 3273. https://doi.org/10.3390/rs14143273.

Zhu, Z., Liao, H., Tu, H., Duan, X., Zhao, Y., 2022. Spaceborne atom-interferometry gravity gradiometry design towards future satellite gradiometric missions. Aerospace 9, 253. https://doi.org/10.3390/aerospace9050253.

Zinage, V., Zinage, S., Bettadpur, S., Bakolas, E., 2024. Leveraging gated recurrent units for iterative online precise attitude control for geodetic missions.

Zingerle, P., Gruber, T., Pail, R., Daras, I., 2024. Constellation design and performance of future quantum satellite gravity missions. Earth Planets Space 76, 101. https://doi.org/10.1186/s40623-024-02034-3.